Atmos. Chem. Phys. Discuss., 9, 15125–15179, 2009
www.atmos-chem-phys-discuss.net/9/15125/2009/

Atmospheric Chemistry and Physics Discussions

This discussion paper is/has been under review for the journal *Atmospheric Chemistry and Physics (ACP)*. Please refer to the corresponding final paper in *ACP* if available.

Observations of boundary layer, mixed-phase and multi-layer Arctic clouds with different lidar systems during ASTAR 2007

A. Lampert[1], C. Ritter[1], A. Hoffmann[1], J.-F. Gayet[2], G. Mioche[2], A. Ehrlich[3,*], A. Dörnbrack[4], M. Wendisch[3,*], and M. Shiobara[5]

[1]Alfred Wegener Institute for Polar and Marine Research, 14473 Potsdam, Germany
[2]Laboratoire de Météorologie Physique UMR 6016 CNRS/Université Blaise Pascal, France
[3]Johannes Gutenberg-University Mainz, Institute for Atmospheric Physics, 55099 Mainz, Germany
[4]Institute of Atmospheric Physics, DLR Oberpfaffenhofen, 82234 Oberpfaffenhofen, Germany
[5]National Institute of Polar Research, Tokyo 190-8518, Japan
[*]now at: Leipzig Institute for Meteorology (LIM), University of Leipzig, 04109 Leipzig, Germany

Received: 28 June 2009 – Accepted: 29 June 2009 – Published: 13 July 2009

Correspondence to: A. Lampert (astrid.lampert@awi.de)

Published by Copernicus Publications on behalf of the European Geosciences Union.

Abstract

During the Arctic Study of Tropospheric Aerosol, Clouds and Radiation (ASTAR), which was conducted in Svalbard in March and April 2007, tropospheric Arctic clouds were observed with two ground-based backscatter lidar systems (micro pulse lidar and Raman lidar) and with an airborne elastic lidar. An increase in low-level (cloud tops below 2.5 km) cloud cover from 51% to 65% was observed above Ny-Ålesund during the time of the ASTAR campaign. Four different case studies of lidar cloud observations are analyzed: With the ground-based Raman lidar, a pre-condensation layer was observed at an altitude of 2 km. The layer consisted of small droplets with a high number concentration (around 300 cm^{-3}) at low temperatures (−30°C). Observations of a boundary layer mixed-phase cloud by airborne lidar were evaluated with the measurements of concurrent airborne in situ and spectral solar radiation sensors. Two detailed observations of multiply layered clouds in the free troposphere are presented. The first case was composed of various ice layers with different optical properties detected with the Raman lidar, the other case showed a mixed-phase double layer and was observed by airborne lidar.

The analysis of these four cases confirmed that lidar data provide information of the whole range from subvisible to optically thick clouds. Despite the attenuation of the laser signal in optically thick clouds and multiple scattering effects, information on the geometrical boundaries of liquid water clouds were obtained. Furthermore, the dominating phase of the clouds' particles in the layer closest to the lidar system could be retrieved.

1 Introduction

The Arctic is considered to be a sensitive indicator of climate change due to a large number of special interactions and feedback mechanisms (Curry et al., 1996). Therefore, data collection by ground-based and airborne experiments in this remote region

ACPD

9, 15125–15179, 2009

is important (IPCC, 2007). Of all atmospheric constituents, water is the most variable in space and time and occurs in all three thermodynamic phases. Clouds have a significant influence on the solar and terrestrial radiation budget. The formation, evolution and dissipation of tropospheric clouds in the Arctic are not yet entirely understood. Unique Arctic cloud characteristics include the occurrence of liquid and mixed-phase clouds at temperatures down to −34°C (Intrieri et al., 2002a; Turner, 2005) and the formation of multiple cloud layers (Verlinde et al., 2007; Luo et al., 2008). Especially, mixed-phase clouds, occurring frequently in the Arctic from spring to fall (Intrieri et al., 2002a), are challenging to describe and parameterize (e.g. Harrington et al. 1999; Morrison et al. 2008). Their impact on the surface radiation balance is difficult to quantify as liquid and solid cloud phases generally show different scattering properties (McFarquhar and Cober, 2004). Further, the radiative effect of mixed-phase clouds depends on their microphysical properties as well as on solar zenith angle and on the surface albedo (Harrington, 1999; Vavrus, 2004). For most of the year, Arctic clouds have a total net warming effect on the surface radiation balance (Curry et al., 1993; Intrieri et al., 2002b), with a mean additional irradiance estimated as 30 $W m^{-2}$ by Intrieri et al. (2002b) and 40–50 $W m^{-2}$ by Curry et al. (1996). However, the local radiative forcing of mixed-phase clouds depends on the partitioning of liquid and ice water in the clouds and can result in a surface cooling of −160 $W m^{-2}$ for pure liquid water clouds (Ehrlich, 2009).

The current cloud parameterizations applied in most regional climate models (e.g. HIRHAM4, Christensen et al., 1996; acronym composed of HIRLAM, High Resolution Limited Area Model, and ECHAM, European Centre for Medium-Range Weather Forecasts, Hamburg), as well as general circulation models (e.g. the National Center for Atmospheric Research Community Climate System Model, NCAR CCSM3, Collins et al., 2006) diagnose the liquid and ice fraction of mixed-phase clouds as a function of temperature. However, measurements show that mixed-phase clouds cannot always be represented adequately by a temperature proxy alone (Pinto et al., 2001; Korolev et al., 2003; Boudala et al., 2004; Mc Farquhar et al., 2007). As a consequence, the

ACPD
9, 15125–15179, 2009

frequently observed existence of liquid droplets at temperatures below 255 K (−18°C, e.g. Turner, 2005) is underestimated by regional climate models (Sandvik et al., 2007), weather prediction models (Gayet el al., 2009) and general circulation models (Vavrus, 2004).

The cloud cover in the Arctic, monitored during the one-year Surface Heat Budget of the Arctic Ocean experiment (SHEBA, Intrieri et al., 2002a), was found to be 85% on average. About 73% of these cases contained at least some liquid water clouds (Intrieri et al., 2002a). Liquid water occurred up to altitudes of 6.5 km (Intrieri et al., 2002a).

Mixed-phase clouds have a characteristic vertical structure consisting of a liquid-dominated layer on top and ice crystals below (e.g. Pinto et al., 1998; Shupe et al., 2008). They have been investigated in a number of campaigns in the North American part of the Arctic: Mixed-Phase Arctic Cloud Experiment, M-PACE, in fall 2004 (Shupe et al., 2007); First International Satellite Cloud Climatology Project Regional Experiment Arctic Cloud Experiment, FIRE ACE, in May/July 1998 (Curry et al., 2000; Lawson et al., 2001); SHEBA in 1997–1998 (Intrieri et al., 2002a, b; Turner, 2005); Beaufort and Arctic Storms Experiment, BASE, in September/October 1994 (Curry et al., 1997; Pinto et al., 1998). Similar extensive ground-based and airborne data sets for the European Arctic are missing. Here, studies of mixed-phase clouds have been performed during the Arctic Study of Tropospheric Aerosol, Clouds and Radiation (ASTAR) near Spitsbergen in June 2004 and March/April 2007 (Gayet et al., 2007, 2009). Further, Arctic clouds were studied during the Polar Study using Aircraft, Remote Sensing, Surface Measurements and Models, of Climate, Chemistry, Aerosols, and Transport (POLARCAT) campaigns from Northern Sweden in April 2008 and Greenland in July 2008 (Law et al., 2008). Due to different possible pollution pathways (Stohl, 2006) and different ambient conditions (especially the western part of Spitsbergen being warm for its location, caused by the influence of the North Atlantic Current) it is not clear whether findings from the North American part of the Arctic can be applied there.

Processes in mixed-phase clouds, ensuring their persistence over days and some-

ACPD
9, 15125–15179, 2009

times weeks, are still poorly understood (e.g. Harrington et al., 1999; Morrison et al., 2008). Their life time critically depends on temperature, ice concentration and also the habit of the ice crystals (Harrington et al., 1999). Evidently, updrafts combined with the availability of water vapor are necessary for their formation and stability (Korolev and Isaac, 2003; Shupe et al., 2007; Korolev and Field, 2008). However, Jiang et al. (2000) and Morrison et al. (2008) showed that the number of ice forming nuclei and the ice concentration are crucial to maintain the mixed-phase clouds in their numerical simulations. Otherwise, the clouds dissipate quickly if the ice concentration gets too high and the ice crystals grow at the expense of the liquid water droplets (Wegener-Bergeron-Findeisen process).

Usually, a temperature inversion above the cloud layers is associated with the existence of these boundary layer clouds (Curry et al., 1997).

Gayet et al. (2007) observed the feeder-seeder effect, i.e. ice crystals and drizzle particles falling out of a cirrus cloud layer into a stratiform liquid droplet cloud layer. This effect can lead to local glaciation of low level clouds with subsequent precipitation of ice crystals and cloud dissipation (Campbell and Shiobara, 2008).

Both in situ measurements and remote sensing observations are crucial in order to obtain a reliable description of cloud properties and their radiative effects. Despite the difficulties to assess the properties of Arctic clouds by satellite observations with little contrast to the snow and ice covered surface (Curry et al., 1996), the evaluation of satellite data (e.g. Key and Intrieri, 2000) plays a key role in the remote Arctic region. Active remote sensing instruments as the lidar provide a two-dimensional cross section of the atmosphere, i.e. information on the vertical and horizontal structure, the homogeneity and the thermodynamic phase of the clouds.

In this article we investigate selected tropospheric Arctic clouds observed during the ASTAR 2007 campaign. Three lidar systems were deployed for the following specified purposes: The ground-based micro pulse lidar (MPL) provided continuous backscatter information on cloud structures 24 h per day. The ground-based Koldewey Aerosol Raman Lidar (KARL) served to determine the backscatter and extinction coefficients

for optically thin clouds. Both lidar systems were situated in Ny-Ålesund. The Airborne Mobile Aerosol Lidar (AMALi), operating in either nadir or zenith viewing direction, was utilized to obtain the backscatter coefficient and depolarization ratio for tropospheric clouds over the Arctic Ocean.

Section 2 introduces the lidar systems and additional airborne instrumentation. The results and analyses of the cloud observations are presented in Sect. 3. A statistical overview of cloud occurrence and height distribution in Ny-Ålesund is presented, followed by a detailed analysis of four selected cloud observations. The two cases A and B describe clouds in the boundary layer, and the remaining two cases C and D clouds in the free troposphere. On the basis of the four separate studies, Sect. 4 provides a discussion of cloud properties which can be derived from lidar data even under the influence of multiple scattering and attenuation of the laser pulses. Section 5 presents a summary emphasizing the importance of lidar as a tool for cloud investigation.

2 Instruments and data

The technical specifications of the three lidar systems, including the typical vertical and temporal resolutions of each instrument, are given in Table 1. In the following, detailed specifications and information on the data evaluation are presented for each lidar system and the additional airborne instruments.

2.1 Micro Pulse Lidar

The micro pulse lidar (MPL) is a compact and eye-safe lidar system for the acquisition of long-term data of particle backscatter profiles on a 24 h basis (Spinhirne, 1993). The MPL in Ny-Ålesund (West coast of Spitsbergen at 78.9° N and 11.9° E) is operated by the Japanese National Institute of Polar Research (NIPR) as a Micro-Pulse Lidar Network (MPLNET, Welton et al., 2001) site in the Arctic. It is maintained by the base personnel of the French-German research station AWIPEV (Alfred Wegener

ACPD
9, 15125–15179, 2009

Institute/Institut Paul Emile Victor).

The system consists of a Nd:YLF laser with a wavelength of 523.5 nm, a signal control unit, a Schmidt-Cassegrain telescope with 20 cm diameter for laser transmission and receiving and a computer for data acquisition. The data is acquired over a sampling range of 60 km with a vertical resolution of 30 m and a temporal average of 1 min. The laser pulses are emitted vertically through a glass window. Data losses usually only occur when the window is covered with snow, which is removed manually.

For the MPL cloud cover statistics of cloud base and cloud top height, the data from 15 March until 30 April was analyzed. First, the data was averaged to means of 10 min, background corrected and cut above 21 km. From the obtained profiles the backscattering ratio (BSR) was calculated with the Klett algorithm (Klett, 1985). The BSR for a given wavelength λ at range z is defined as

$$\mathrm{BSR}(\lambda, z) = \frac{\beta^{\mathrm{Ray}}(\lambda, z) + \beta^{\mathrm{part}}(\lambda, z)}{\beta^{\mathrm{Ray}}(\lambda, z)}, \quad (1)$$

where β^{Ray} and β^{part} are the molecular Rayleigh and the particle backscatter coefficients, respectively.

Using different thresholds for the difference between two adjacent BSR values (high values above 0.1 increasing for at least 3 height steps or a single peak difference of minimal 0.2 to 0.3 if no lower clouds were detected), the BSR was analyzed for cloud peak structures in five distinct altitude intervals: 0–300 m (snow on the window), 300–1200 m (boundary layer clouds), 1200–2500 m (low clouds), 2500–5500 m (midlevel clouds) and 5500–10 000 m (high clouds). If none of these were detected the profile was set to "cloud free". The cloud categories take into account the frequent occurrence of two temperature inversions at around 1200 m and 2500 m altitude observed by radio sounding in Ny-Ålesund, which is influenced by local orography. The upper limit of midlevel clouds follows the definition of Pinto et al. (2001).

Since the signal to noise ratio (SNR) above a cloud structure can decrease dramatically, the peak threshold conditions were adjusted accordingly (e.g. a SNR below 3

ACPD
9, 15125–15179, 2009

between 7.5 and 10 km and the detection of no clouds give evidence that there was snow on the window instead of a cloud free atmosphere). Depending on the optical thickness of the lower clouds, the data about the occurrence of higher clouds have to be considered as less reliable.

2.2 Koldewey Aerosol Raman Lidar

The Koldewey Aerosol Raman Lidar (KARL), firmly integrated in the atmospheric observatory at Ny-Ålesund, measures aerosol, clouds and water vapour in the troposphere and aerosol in the stratosphere. In 2007, it consisted of a Spectra Nd:YAG laser emitting at the wavelengths 355 nm, 532 nm and 1064 nm simultaneously at a pulse repetition frequency of 50 Hz and a power of about 10 W per wavelength. The telescope of 30 cm diameter with 0.83 mrad field of view (FOV) shows a complete overlap above 1.2 km. It collects, apart from the mentioned elastic wavelengths (532 nm also in perpendicular state of polarization), the molecular nitrogen Raman shifted lines at 387 nm and 607 nm, as well as the water vapor lines at 407 nm and 660 nm. For the lowest atmospheric layers, a smaller mirror of 11 cm diameter with 2.25 mrad FOV was used, which provided information above an altitude of 500 m. In this range, only the wavelengths 532 nm, 607 nm and 660 nm were recorded. More details about the system and its applications can be found in Ritter et al. (2004). Combining the backscatter at 3 wavelengths and extinction at 2 wavelengths, KARL data can be used to estimate the index of refraction and the size distribution for spherical particles in the range between 0.1 µm to 1.25 µm following the method developed by Böckmann (2001).

The analysis of the lidar data was performed in the following steps:

First the lidar profiles were averaged to a resolution of 10 min and 60 m. The retrieval of the extinction from remote sensing data is a mathematically ill-posed problem (Pornsawad et al., 2008) and any kind of smoothing would strongly affect the derived extinction. Therefore, the extinction of the molecular nitrogen Raman signals at 387 nm and 607 nm was calculated according to the method by Ansmann et al. (1992) for completely unsmoothed lidar signals. Due to the inevitable noise in the data, the extinction

ACPD
9, 15125–15179, 2009

coefficient was not calculated directly but its average over the height interval containing the cloud of interest.

The KARL and MPL lidar systems were compared for one particular day (21 April, cloud C).

For the same temporal and vertical resolution, a SNR of around 5 was obtained at 15 km altitude by KARL and at 5 km altitude by the MPL. Therefore, the KARL lidar is better suited for the observation of optically thin and high clouds. However, it cannot detect optically thick clouds if the detectors are saturated. In contrast, the MPL was designed in a way that also the detection of optically thick clouds is possible.

2.3 Airborne Mobile Aerosol Lidar

The Airborne Mobile Aerosol Lidar (AMALi) is an airborne backscatter lidar system operating at two wavelengths (532 nm and 355 nm) with additional depolarization measurements at 532 nm (Stachlewska et al., 2004; Lampert et al., 2009; Stachlewska et al., 2009). AMALi has been developed and operated by the Alfred Wegener Institute for Polar and Marine Research (AWI). The real time display of the range corrected lidar signal offers the possibility to detect atmospheric structures of interest during the flight and guide the aircraft accordingly. In this paper, we focus on the signal at the wavelength of 532 nm in both polarization directions. No supplementary information was retrieved from the second wavelength of 355 nm considering cloud particles with diameter larger than the lidar wavelengths (effective diameter >5 µm). AMALi can be installed in nadir or zenith looking configuration. The minimum horizontal resolution was determined by a signal to noise ratio above 15 at cloud top in nadir and at cloud base in zenith configuration. For the cases presented here, the data were averaged over 15 s. At the aircraft's ground speed of about 60 m s^{-1}, the horizontal resolution was around 900 m. The evaluation of the lidar data was done with the standard Klett algorithm (Klett, 1985). In the inversion algorithm, a value of the backscatter has to be assumed at the far end of the lidar profile. For the nadir measurements of optically thick boundary layer clouds, this value was set within the clouds and varied iteratively

ACPD
9, 15125–15179, 2009

to obtain a reasonable backscatter ratio above the cloud. However, for optically thick clouds, it is not possible to derive accurate values of the cloud backscatter and extinction coefficients from the lidar measurements. Only qualitative information about the structure and the thermodynamic phase of the uppermost cloud layer can be obtained in this case. For the zenith measurements of optically thinner midlevel clouds, the fit value was set above the clouds and varied iteratively to obtain plausible values of the backscatter in the free troposphere below the cloud. The air density profiles necessary for estimating the Rayleigh backscatter profiles were computed from meteorological data of the temporally closest radio sonde launched from the AWIPEV observatory in Ny-Ålesund.

Information from the depolarization channel has to be considered carefully. In the case of optically thick clouds, multiple scattering occurs and modifies the depolarization signal. As the FOV of the AMALi is rather large (3.1 mrad), multiple scattering affects the lidar signal for clouds with an optical depth higher than 0.1. With increasing optical depth, the depolarization signal received from liquid clouds increases gradually from 0 to values in the range of non-spherical ice particles (e.g. a depolarization ratio of 30% at an optical depth of around 3 was calculated for the geometry of the Cloud-Aerosol Lidar with Orthogonal Polarization, CALIOP, You et al., 2006). However, in the case of ice crystals, the depolarization signal increases instantaneously at cloud top. Therefore, the slopes of individual AMALi profiles of backscatter and depolarization ratio were evaluated in order to distinguish whether a cloud layer consisted of liquid water droplets or ice particles.

2.4 Additional airborne instruments

2.4.1 In situ measurements

The different in situ instruments deployed on board of the Polar-2 were operated by the Laboratoire de Météorologie Physique (LaMP). They included the Forward Scattering Spectrometer Probe (FSSP-100, Dye and Baumgardner, 1984; Gayet et al., 2007), the

ACPD
9, 15125–15179, 2009

Cloud Particle Imager (CPI, Lawson et al., 1998) and the Polar Nephelometer (PN, Gayet et al., 1997). The systems provided measurements of particle number concentration, particle extinction coefficient, ice and liquid water content, effective diameter of the particles, particle phase function, and asymmetry parameter. The FSSP is sensitive to the typical size of liquid water droplets up to 45 µm. The CPI covers the particle sizes between 23 µm and 2300 µm with a resolution of 23 µm. The PN is sensitive to cloud particles in the size range of about 3 µm to 800 µm. It measures an ensemble of both liquid and ice particles. The retrieval of PN data is described by Oshchepkov et al. (2000) and Jourdan et al. (2003). From PN data, the particle asymmetry parameter g is determined, with θ being the scattering angle and P the phase function:

$$g = <\cos\theta> = \frac{1}{2}\int_{-1}^{1} \cos\theta \cdot P(\cos\theta) \cdot \mathrm{d}\cos\theta \,. \quad (2)$$

It is used to discriminate between nonspherical (ice crystals, g<0.82) and spherical particles (liquid water droplets, g>0.82).

2.4.2 SMART-Albedometer

The Spectral Modular Airborne Radiation measurement sysTem (SMART-Albedometer) operated by the University of Leipzig measures downwelling spectral irradiance $F_\lambda^\downarrow$ and upwelling nadir radiance $L_\lambda^\uparrow$ in the visible (350–1000 nm) and near-infrared range (1000–2100 nm). It is actively horizontally stabilized for airborne applications (Wendisch et al., 2001). A detailed description of the SMART-Albedometer configuration during ASTAR 2007 is presented by Ehrlich et al. (2008). From the measurements, the spectral cloud top reflectance

$$R_\lambda = \pi L_\lambda^\uparrow / F_\lambda^\downarrow \quad (3)$$

ACPD
9, 15125–15179, 2009

is determined. Further, the spectral slope ice index I_S as introduced by Ehrlich et al. (2008) was analyzed in order to distinguish the cloud phase. It is defined by

$$I_S = \frac{100}{R_{1640\,\mathrm{nm}}} \cdot \left[\frac{dR}{d\lambda}\right]_{[1550\,\mathrm{nm},1700\,\mathrm{nm}]} . \quad (4)$$

Values below 20 indicate liquid water clouds.

Additionally, the cloud optical thickness is estimated by the method presented by Nakajma and King (1990) assuming liquid water clouds. The accuracy of the cloud optical thickness derived from the uncertainties of the measurements decreases with increasing optical thickness. The error is below 20% for clouds with an optical thickness of less than 20.

3 Cloud observations

An overview of the cloud occurrence at different altitudes is provided in Sect. 3.1. The following four specific case studies are presented in Sects. 3.2 to 3.5:

A) an optically thin layer of pre-condensed liquid droplets at low temperatures observed with the ground-based Raman lidar at an altitude of 2 km.

B) a boundary layer mixed-phase cloud observed by airborne lidar in nadir configuration.

C) an ice cloud in the free troposphere consisting of several ice layers observed with the ground-based Raman lidar.

D) a cloud with double-layer structure and mixed-phase conditions in the free troposphere probed by airborne lidar in zenith configuration.

For each case, the properties making it noticeable are further analyzed.

ACPD
9, 15125–15179, 2009

3.1 MPL statistics of clouds during ASTAR 2007

3.1.1 Results

As an overview of the general cloud situation in Svalbard during the ASTAR 2007 campaign, MPL cloud analyses are presented. The main finding for the period of 15 March to 30 April 2007 is a significant increase of boundary layer and low level clouds through the analyzed time period from 51% to 65% (Fig. 1). The occurrence of clouds below 1200 m even increased from about 36% in the second half of March to 59% in the second half of April, while the clear sky fraction remained roughly constant at about 25% to 33%.

3.1.2 Analysis

Regularly, the cloud cover in the Arctic grows with sunlit season (Key et al., 2004). During the transition period in spring, a strong increase in low-level cloud cover is observed. Our Ny-Ålesund results of increasing cloud cover for spring 2007 are similar to the MPL observations of Shiobara et al. (2003) for March and April 2002. Furthermore, ceilometer measurements in Ny-Ålesund documented an increase of low lewel cloud cover (0–2 km) from 30% in March to 50% in April 2001 (Kupfer et al., 2006). The cloud statistics presented here indicate that the atmospheric conditions of a typical Arctic spring were present in 2007.

This is of special interest as the Arctic haze phenomenon with enhanced tropospheric aerosol load was not pronounced during the ASTAR 2007 time period (Hoffmann et al., 2009). Arctic haze, observed regularly at Ny-Ålesund by sun photometer (Herber et al., 2002) and lidar (Ritter et al., 2004) in spring time, occurs often at altitudes below 3 km (Scheuer et al., 2003) and provides cloud condensation nuclei for cloud formation. Despite the absence of Arctic haze, the increase in low level cloudiness was observed. However, even under clean conditions, particles in the accumulation mode were found in Svalbard throughout fall to spring (e.g. Ström et al., 2003). They were

ACPD
9, 15125–15179, 2009

subject to long-range transport and perseverate sometimes over months in the Arctic atmosphere (Ström et al., 2003). Also sea salt particles of local origin serve as cloud condensation nuclei. The thawing of sea ice and the increased solar radiation in spring leads to more water vapor in the atmosphere available for cloud formation.

The following selected cases from ASTAR 2007 describe particular clouds which formed under relatively clean ambient conditions in the Arctic.

3.2 KARL observation of a layer of pre-condensed liquid droplets in the boundary layer (case A)

3.2.1 Results

With the ground-based lidar KARL, a 6 h observation was performed in Ny-Ålesund during local afternoon/evening on 19 April 2007. Figure 2 shows an overview of the particle backscatter coefficient up to the tropopause level. In the lidar data, a persistent but optically subvisible cloud at 7.5 km altitude and another one around 5 km altitude between 18:00 and 21:00 UTC was observed. However, in this study, the layer of enhanced backscatter and very low depolarization around 2 km altitude is discussed in detail (case A). We analyze in the following whether the layer consisted of liquid water droplets and thus merits the name "cloud", or whether we observed an aerosol layer.

Figure 3 (left panel) shows the profiles of backscatter and depolarization ratio in the height interval including the layer of interest at 16:55 UTC. The volume depolarization is very close to the background value of 1.4% (typical for air molecules) within the layer and only increases slightly to 1.9% at 2 km altitude, right above the layer. Hence apart from a shallow layer on top, the particles of case A are spherical in shape.

A radio sonde, launched in Ny-Ålesund at around 11:00 UTC, revealed high values of relative humidity (>90%) between 1.8 and 2.5 km altitude, which confirms the possible existence of a cloud. Further, the sonde revealed a low temperature of 244 K (−29°C) at 2 km and a week inversion of 1.5 K with a minimal temperature of 241 K (−32°C) at 2.5 km altitude (Fig. 3, right panel).

ACPD
9, 15125–15179, 2009

With the density profile of the radio sonde, the backscatter coefficient was derived in 10 min temporal and 60 m vertical resolution (Ansmann et al., 1992). The optical depths of case A were determined to be 0.0633 for 355 nm and 0.0348 for 532 nm at 16:55 UTC. For this time, an average lidar ratio (LR, defined as the extinction to backscatter ratio) of 26.2 (±3) sr for 355 nm and 20.2 (±6) sr for 532 nm was derived for the whole layer. As the low level layer dissolves after 19:00 UTC (Fig. 2), the LR increases slightly in both wavelengths (not shown). For a fixed chemical composition, a higher LR for spherical particles is related to smaller diameters (Ackermann, 1998).

3.2.2 Analysis

The low depolarization values of case A show that the backscattering particles were spherical. This is an indication of the presence of liquid water droplets. In contrast, all Arctic haze events over Spitsbergen observed by KARL since 2000 showed a depolarization between 2 and 4% (Hoffmann et al., 2009).

As the sphericity of the particles is evidenced by the depolarization measurements, the scattering properties can be described by Mie theory. The backscatter and extinction coefficients decreased with wavelength, which suggests that the scattering particles were predominantly of sub-micron size, thus typical of aerosol. An inversion of the lidar data (backscatter at 3 wavelengths and extinction at 2 wavelengths, Böckmann, 2001) to derive the microphysical properties was performed. We used the inversion code originally developed by Kirsche and Böckmann (2006) for aerosol size retrieval from lidar data. It seeks the volume distribution function of spherical scatterers of size smaller than 1.25 µm which matches to the lidar extinction and backscatter coefficients in an optimal way. It must be stated here that possibly particles larger than 1.25 µm may exist as well. As particles which are much larger than the lidar wavelengths become "grey" – meaning that their scattering properties do not depend on wavelength by large amounts – no information on their size distribution can be obtained in that case. However, in case A, the backscatter and extinction coefficients are clearly decreasing with wavelengths indicating that the main part of the particles was smaller than 1.25 µm.

ACPD
9, 15125–15179, 2009

The results of the inversion are presented in Fig. 4, showing the volume distribution function in dependence of the particle radius. Two modes of particle sizes can be distinguished, the smaller one with an effective radius of around 280 nm and high particle number concentration (290 cm^{-3}), and the larger one with an effective radius of around 740 nm and low particle number concentration (7 cm^{-3}). This particle size range is typical of aerosol in the accumulation mode. However, the size distribution of pre-condensation droplets also includes particles in the sub-micro range (e.g. Tomasi and Tampieri, 1976). Usually, Arctic cloud droplets have a larger effective radius in the range of 10 µm for temperatures around −20°C (e.g. Gayet et al., 2009).

The volume distribution function (Fig. 4, blue curve) can be fitted by a bimodal lognormal size distribution (green curves). The index of refraction was retrieved as $1.43+5\times10^{-4}$i for the wavelength of 532 nm.

The determination of a precise index of refraction from lidar data is challenging (Kirsche, 2008) as no direct information on absorption is available, which determines the imaginary part. However, a low real part value, only slightly higher than that for pure water droplets (1.33, d'Almeida et al., 1991) was found. This index of refraction is significantly lower than the values derived for Arctic haze events with the same instrumentation (exceeding 1.5, Hoffmann et al., 2009).

The effective radii of the bimodal log-normal size distribution as well as the total particle volume are found to be almost insensitive to changes in the real part of the refractive index. However, there is a dependence on the imaginary part of the refractive index: if it is artificially set to a larger value of 2×10^{-3}, which is the maximum value compatible with our calculations in the inversion code and typical of aerosol, the mode of large particles around 0.77 µm becomes the dominant one. The low refractive index and depolarization indicate the existence of liquid pre-condensation droplets. Therefore, under the assumption that all of the scattering particles only consist of pure water, a total liquid water amount of 1.21×10^{-5} g m^{-3} in the thickest part of the cloud was derived (the total particle volume can be retrieved to a precision of 10%). Later, at 21:12 UTC, the higher lidar ratio is translated into a decrease of the mode of the larger

ACPD
9, 15125–15179, 2009

droplets.

Using the pressure and relative humidity from the radio sonde several hours earlier, a maximum water vapor content of 0.66 g m^{-3} was observed around 2 km altitude. This means that even considering a pronounced temporal change of the water vapor content (for example a drying – which is unlikely due to the cloud presence in the afternoon), the vast majority of the water must be confined in the gas phase.

To further differentiate if we detected water droplets or aerosol, HYbrid Single-Particle Lagrangian Integrated Trajectory (HYSPLIT, Draxler and Hess, 1998) arriving at 17:00 UTC over the AWIPEV base were analyzed to interpret the inversion of the lidar data and obtain information on the possibility of pollution (not shown). The temperature (HYSPLIT gives 247 K at 2 km altitude) and the high relative humidity in the cloud layer hardly changed between the launch of the Vaisala RS-92 sonde at 11:13 UTC and the time of the lidar observation. Until 2 days prior to their arrival the air masses were trapped in the boundary layer, 6 days before they reached the Siberian coast. However, after arriving over the Arctic Ocean, a small amount of about 0.6 mm precipitation was simulated. This reveals that even if the air had taken up some pollutant over northern Siberia it might have lost it 4 days prior to its arrival over Spitsbergen. The last precipitation occurred 2 days before from the 1700 m trajectory during its updraft (0.5 mm). Any possible contamination of the air mass with hygroscopic aerosol should have led to the growth and removal of the particles at that stage. On the other hand, possible insoluble components as for example soot particles are neither spherical nor show a low refractive index.

Generally during the ASTAR 2007 campaign, clean air was recorded by sun photometer and lidar measurements in Ny-Ålesund during the whole month of April (Hoffmann et al., 2009). Therefore, the low index of refraction obtained by the lidar data inversion was most likely caused by supercooled pre-condensed liquid droplets. However, we cannot totally exclude the existence of some hygroscopic aerosol contamination (Korhonen et al., 1996).

Contrary to the findings presented here, Arctic haze events normally have an en-

ACPD
9, 15125–15179, 2009

hanced volume depolarization (Ishii et al., 1999), show a higher index of refraction (d'Almeida et al., 1991), show only a mono-modal log-normal distribution (Ström et al., 2003) and flow in drier air (Ishii et al., 1999). During the observation period, a small part of the particles might have been activated to cloud droplets, as indicated by the increasing LR, which can be interpreted as the disappearing larger mode in the lidar data inversion. The large cloud droplets have a negligible scattering coefficient in the visible wavelengths compared to accumulation mode particles (e.g. Komppula et al., 2005), and they have the same scattering effect for all the lidar wavelengths. As only few particles are activated, the remaining pre-condensed particles dominate the lidar signal. Hence, we interpret the lidar observations of case A as a layer consisting mainly of supercooled pre-condensed liquid particles at low temperatures.

3.3 AMALi observation of mixed-phase boundary layer clouds (case B)

3.3.1 Results

Airborne observations of mixed-phase boundary layer clouds were conducted on 9 April 2007. The flight path was synchronized with the Cloud-Aerosol Lidar and Infrared Pathfinder Satellite Observations (CALIPSO) track above the open Greenland Sea (Gayet et al., 2009). Lidar measurements were performed during the first part of the flight in North-West direction at an altitude of 2760 m from 08:36 to 09:25 UTC (case B). On the way back, in situ profile measurements were performed within the clouds from 09:50 to 10:44 UTC. The CALIPSO overflight took place at 10:06 UTC. The meteorological situation, analyzed in detail by Richter et al. (2008) and Gayet et al. (2009), revealed the existence of two different air masses. Convective cloud rolls and northerly flow with low temperatures were observed in the southern part of the flight track, and warmer air with scattered clouds in the northern part of the flight track.

In Fig. 5, the time series of lidar backscatter profiles is shown. The two different air masses can clearly be distinguished. During the first part of the lidar flight (08:40–08:57 UTC), a continuous cloud deck with high values of the backscattering ratio (ex-

ACPD
9, 15125–15179, 2009

ceeding 50) was observed. The cloud top was rising with increasing boundary layer height, as confirmed by ECMWF analyses (Richter et al., 2008). Structures of high backscattering were seen below the liquid layer for most time steps, i.e. the ground return and liquid layer down to the lower liquid cloud boundary. In the second part of the lidar flight, after 09:02 UTC, scattered clouds at different altitudes were present. In this part, the ground return of the lidar signal was mostly visible through the clouds (Fig. 5).

The time series of the depolarization ratio is presented in Fig. 6. The data exhibit mainly values of around 10%. However, in the mixing zone of the different air masses at around 09:02 UTC, the depolarization was found to be significantly higher (up to 20%).

Exemplary individual profiles of backscattering ratio and depolarization ratio for two times (08:48 and 09:03 UTC) are shown in Fig. 7. They exhibit different characteristics concerning the values and slopes of the profiles. A high backscattering ratio exceeding 30 and gradual increase of the depolarization up to 8% with cloud penetration depth was found for the time representative of the continuous cloud deck at 08:48 UTC. A much lower backscattering ratio of 15 and a higher value of the depolarization ratio of 20%, enhanced immediately at the cloud top, were observed in the air mass mixing zone. This indicates a liquid water cloud top layer at 08:48 and an ice cloud at 09:03 UTC.

The temperature profiles obtained during the subsequent in situ measurements are shown in Fig. 8. During the northern part of the in situ leg oriented in South-East direction (blue color), the temperature was around −12°C at the altitude of 550 m, and −21°C at 1500 m. After 10:18 UTC, in the southern part of the flight, the temperature below 1100 m was about 1.5 K colder (green color).

3.3.2 Analysis

In the following, a comparison of the lidar data with albedometer and in situ observations is given. Specific analyses concerning the reliability of lidar to observe the cloud structure and cloud phase are performed in Sect. 4.

ACPD
9, 15125–15179, 2009

Assuming pure water clouds, the cloud optical thickness estimated from albedometer data shows values around 13–17 for the more homogeneous cloud deck in the South. In the mixing zone starting at 09:00 UTC, the optical thickness was lower (11–13 assuming pure ice).

In situ measurements were performed at a flight altitude between 200 m and 1600 m during ascents and descents in the clouds. They are described in detail by Gayet et al. (2009). A thick water layer of around 500 m thickness was observed at cloud top. The FSSP showed a mean effective diameter of 20 µm and a concentration of more than 50 cm^{-3}. PN measurements revealed an extinction coefficient up to 35 km^{-1}. Below, ice crystals were observed. The CPI showed an effective diameter of up to 300 µm and a concentration of more than 400 l^{-1}. The extinction coefficient was typically below 5 km^{-1}. The AMALi observations of cloud case B agree with the in situ measurements concerning the optically thick liquid cloud layer on top. However, it was not possible to observe the ice crystals below, as the laser beam was attenuated. As mentioned above, only structures of high backscattering were seen below the liquid layer. Due to the time delay and the flight pattern during the in situ probing, the cloud altitudes cannot be compared directly.

The spectral slope ice index I_S calculated from the cloud reflectance measurements (Ehrlich et al., 2008) is superposed as red line in the time series of depolarization (Fig. 6). Low values of 10 to 30, indicating water or mixed-phase clouds with predominantly liquid contribution, are characteristic for most of the clouds. In the air mass mixing zone, however, the ice index shows enhanced values up to 50 indicating clouds dominated by ice crystals. This confirms the lidar observation of enhanced depolarization values, characterizing a glaciated cloud.

The nearly simultaneous in situ measurements observed a cloud consisting of ice only at 10:18:30 UTC. As shown in Fig. 9, the asymmetry parameter obtained from the PN was below or close to 0.82 for 15 s (horizontal extent of around 900 m). The data were collected in the mixing zone of the air masses, indicated by the transition of the temperature profiles as described in Sect. 3.3.1.

ACPD
9, 15125–15179, 2009

3.4 KARL observation of a multiple layered midlevel ice cloud (case C)

3.4.1 Results

On 21 April 2007 a cirrus cloud containing up to three different layers was observed by ground-based lidar over Ny-Ålesund from 20:20 to 21:00 UTC (case C). Figure 10 shows a time series of the backscatter coefficient at 532 nm wavelength. The cloud layers are visible between 2.5 and 5 km altitude. This cloud was optically thin, but much denser compared to the liquid pre-condensation layer presented in case A. At 20:30 UTC its optical depth amounted to 0.167 at 532 nm and 0.169 at 355 nm. The according LRs were 33(±2) sr and 18(±1) sr for the respective wavelengths. The cloud consisted purely of ice crystals which showed a very high volume depolarization of up to 70%.

At 20:50 UTC the lidar profiles presented in Fig. 11 (left) exhibited a distinctive internal structure of the cloud. The highest layer showed almost the same particle backscatter of $3\times10^{-6}\,m^{-1}\,sr^{-1}$ for both wavelengths, a value as expected for cirrus. Also the LRs for both wavelengths are similar: 19.8 sr vs. 17.9 sr. This translates into an optical depth of 0.11 for both wavelengths.

However, the subjacent layer between 3 and 3.5 km altitude was accompanied by a minimum of the depolarization of only 10%, and the backscatter was higher in the UV compared to the visible wavelengths. On the other hand, the cloud optical thickness detected in the two wavelengths was comparable (0.25 for 532 nm and to 0.21 for 355 nm). This means that the LR for the UV (6.5 sr) is lower than the LR for 532 nm (14.4 sr).

The lowermost cloud layer at around 2.6 km altitude, which was basically visible in the UV, is striking because it shows a different LR: 37.0(±1) sr for the visible branch, but only 3.0(±0.2) sr for the UV.

ACPD
9, 15125–15179, 2009

3.4.2 Analysis

For this case C, we analyze the optical properties of the cloud system and discuss deductions for the microphysics of the ice crystals. The cloud exhibits the lowest LR measured by KARL during the ASTAR 2007 campaign. Due to this extremely low LR in the UV, the optical depth of the cloud layer at 2.6 km is higher in the visible than in the UV (0.312 vs. 0.216). To prove this finding, the backscatter coefficient and backscatter ratio were additionally calculated with the Klett approach (Klett, 1985) applying the obtained LR. The results were found to be in agreement with the above data calculated with the method presented by Ansmann et al. (1992). Choosing a higher LR in the Klett method produces a physically unrealistic backscatter ratio smaller than 1 below the cloud base. Due to the non spherical shape of the ice cloud particles and their size, a lidar inversion code based on Mie theory cannot retrieve their microphysical properties.

Lidar observations of cirrus clouds have been performed by various groups. A typical LR value for cirrus clouds is around 30 sr at 532 nm wavelength (Chen et al., 2002; Giannakaki et al., 2007). Our observations of the LR at 532 nm agree with these values in the given standard deviation. Reichardt et al. (2002) calculated LR and depolarization of (almost) hexagonal particles in random orientation with a ray tracing code. They found lidar ratios as low as 3 sr, albeit frequently in conjunction with very high depolarization. The values of lidar ratio and depolarization of case C seem to best match with plates of high aspect ratio (Reichardt et al., 2002, their Fig. 7).

As the LR is determined by particle size, shape and aspect ratio of the ice crystals, it depends on the cloud temperature, which favours the formation of different ice crystal habits (Sassen and Comstock, 2001), as well as cooling rates and aerosol properties at ice supersaturation (Haag and Kärcher, 2004). However, simulated backward trajectories show that the air mass investigated here did not pass areas where the uptake of pollution was likely (not shown). The temperature and humidity profile of case C was estimated from radio sounding measurements several hours earlier (Fig. 11, right). At

ACPD
9, 15125–15179, 2009

around 11:00 UTC, the temperature decreased from 248 K (−25°C) at 2.5 km altitude to 234 K (−39°C) at 5 km altitude. However, the shown differences in the optical properties of the cloud, the different LR and the depolarization, are surprisingly large for the temperature range. Korolev et al. (2000) and Bailey and Hallett (2002) showed that irregular ice crystals dominate all temperature intervals of interest here. They observed a high fraction of irregular ice crystals (>85%) in stratiform clouds and by cloud chamber experiments, respectively. Surely, changes in the shape and size of the ice crystals of this cloud system are pronounced. The findings suggest that it is worth identifying similar cloud cases by lidar, and studying the evolution of the ice particle size and shape in combination with in situ probing.

3.5 AMALi observation of a two-layer midlevel cloud (case D)

3.5.1 Results

On 14 April 2007, the Polar-2 aircraft went from Longyearbyen towards the South along the West coast of Svalbard, in the direction of an approaching high pressure system. For a horizontal extent of around 30 km (8 flight minutes) from 16:18 to 16:26 UTC, a two-layer cloud structure was observed by the zenith pointing AMALi (case D). As the aircraft was cruising at constant altitude (1300 m) until 16:24 UTC, only this first part of the lidar backscattering ratio of the cloud is shown in Fig. 12. The signal is smoothed vertically with a running mean over 10 data points, and the time resolution is 15 s. Two separated geometrically thin liquid clouds (150 m vertical extent) with high backscatter ratio and low depolarization were observed (Figs. 12 and 13). The backscatter ratio of the lower layer was smaller than the value of the higher layer at the beginning of the cloud observation. The upper cloud was centered at 4.2 km altitude, the lower cloud at 3.9 km. In between, the enhanced depolarization and low backscatter signal revealed the existence of precipitating ice particles. The temperature at 4 km altitude was estimated with −25°C (radio sonde measurement in Ny-Ålesund at around 11:00 UTC). A cirrus cloud was located above the two-layer cloud system with a slanted cloud base

ACPD
9, 15125–15179, 2009

at around 5.5 km (not shown in Fig. 12). As multiple scattering leads to an enhanced apparent optical depth (Nicolas et al., 1997), only a maximum value for the optical depth can be estimated as follows: The maximum backscatter coefficient of the upper liquid layer was around $10^{-4}\,m^{-1}\,sr^{-1}$. Multiplication of this value with a typical cloud LR of 30 (e.g. Chen et al., 2002) and integration over the cloud altitude (150 m) leads to an estimation of the optical thickness in the order of 0.45, which represents an optically thin cloud. The signal to noise ratio at 4 km altitude amounts to 15.

3.5.2 Analysis

In the following study possible formation processes of the double-layer cloud of case D are analyzed considering the meteorological context. The cloud structure and cloud thermodynamic phase are discussed separately in Sect. 4.

In contrast to multiple cloud layers in the Arctic boundary layer observed regularly in summer (e.g. Intrieri et al., 2002a; Luo et al., 2008), multiple layer clouds in the free troposphere are less frequently reported. A complex multiple layer cloud system with layers up to 5.5 km altitude was analyzed by Hobbs et al. (2001). They found ice crystals falling from the individual cloud layers into lower layers, and at times evaporating above ground.

Meteorological analyses of case D revealed that on the rear side of a through propagating eastward, the low level wind turned from north-westerlies to easterlies in the period from 12:00 UTC till 18:00 UTC. However, the wind speed was rather low with values around $2\,m\,s^{-1}$ at 10 m. The prevailing easterly winds near ground level turned to westerlies at higher pressure levels above Spitsbergen (Fig. 14). Associated with the approaching ridge, warm and moist air was transported to the Svalbard area at the altitude of the cloud observation. As the wind at the aircraft's cruising altitude (1300 m) during the cloud observation came from the west, the lidar observations were performed along a cross section perpendicular to the wind direction prevailing at cloud level.

ECMWF analyses reveal the existence of an area of humid air masses (relative hu-

midity around saturation) at 700 hPa and enhanced relative humidity up to 90% at 500 hPa (Fig. 14, right). Midlevel clouds were analyzed in the observation area. However, the small scale structure of the observed cloud D could not be resolved by the ECMWF analyses.

Different possible mechanisms are responsible for the lifting of the air masses and cloud formation: A possible scenario is that the humid air masses were lifted orographically. Until about 12:00 UTC, westerlies dominated in the lower troposphere and the flow perpendicular to the coast line passed the mountains of the Svalbard archipelago. However, the cloud was observed on the windward side and in the direct vicinity of Svalbard (less than 5 km off land). Therefore, the observed clouds cannot be typical lee wave clouds. Another possible explanation is that the flow above the Svalbard archipelago was interrupted by the change of the wind direction in the lower troposphere. As the forcing of gravity waves diminishes, an upstream shift of the waves might occur under these transient conditions (Chen et al., 2007).

A third possibility is that cloud filaments formed due to the enhanced vertical and horizontal wind shears in the strongly divergent flow. Lifting by one of the mentioned mechanisms and subsequent cooling of the moist air is probably the cause of the formation of at least the upper liquid cloud layer. As precipitation between the individual cloud layers was observed, and the lower liquid cloud layer exhibits a smaller optical thickness, the double-layer structure D might be a result of ice crystal precipitation which evaporated below the upper cloud (as proposed by Harrington et al., 1999). Radiative cooling or further orographic lifting led to cooling of the humid layer, resulting in the second cloud layer.

4 Discussion: retrieval of cloud boundaries and cloud thermodynamic phase from lidar observations

Lidar observations cover the whole range from optically thin to thick clouds at different altitudes. In this section, the information retrieval from lidar measurements is dis-

ACPD
9, 15125–15179, 2009

cussed.

Optically thin to subvisible clouds (i.e. values of the cloud optical depth below 0.03 at 532 nm wavelength, Sassen et al., 1989) can easily be observed with lidar systems (Lampert et al., 2009). In Sect. 3.2, we presented an example of a supercooled precondensation layer (case A) with an optical depth of 0.038 and an estimated water content of 1.21×10^{-5} g m^{-3}, which was located below a subvisible cirrus of even lower optical depth. An optically thin ice cloud consisting of layers with different properties (case C) was described in Sect. 3.4. With the assumption of single scattering being valid, the optically thin clouds (cases A and C) can be characterized by quantitative backscatter efficient and depolarization ratio. This allows a reliable determination of the cloud structure and cloud phase. Raman lidar further provides the extinction coefficient without an assumption of the lidar ratio.

On the other hand, optically thick clouds attenuate the lidar signal and lead to multiple scattering, which influences the detection of backscattered radiation in both polarization directions. The photons which are scattered more than once are detected at a later time, provoking an afterglow effect behind the cloud. The signal strength cannot be evaluated quantitatively within and behind the cloud, but the boundaries of a strongly backscattering cloud can still be observed.

The depolarization of a pure water cloud consisting of spherical droplets is zero for a backscatter angle of 180°, but the depolarization value measured by a lidar system strongly depends on its FOV (Hu et al., 2001). This effect can also be explored by multiple FOV lidar systems to get additional information on the extinction coefficient and the effective diameter of the scattering particles (Bissonnette et al., 2005). For lidar systems with a fixed FOV, the relation of parallel and cross-polarized signals reveals whether the scattering particles are mainly spherical or nonspherical, indicating liquid or ice water. For liquid water clouds, the backscatter and the depolarization are positively correlated, while for ice clouds, the depolarization decreases with penetration into the cloud, as was observed for CALIPSO data (Hu et al., 2006, 2007). You et al. (2006) calculated the behaviour of the depolarization signal in case of non-depolarizing liquid

ACPD
9, 15125–15179, 2009

cloud droplets as a function of the optical depth with Monte Carlo simulations. Ice clouds consisting of different ice particle habits can also be discriminated theoretically, as they have their own starting values and slopes of depolarization as a function of optical thickness (You et al., 2006).

In the case of KARL with a FOV of 0.83 mrad, a BSR >40 at 532 nm wavelength for clouds in 5 km altitude is the limit for which multiple scattering becomes noticeable in the lidar profiles. Thick low clouds (as low as 2 km altitude) have not been analyzed so far due to saturation in the detectors.

As stated in Sect. 2.3, the AMALi has a relatively wide FOV (3.1 mrad), and multiple scattering effects are observed for a cloud optical thickness as low as 0.1. For the evaluation of clouds with higher optical depth, multiple scattering cannot be neglected in this system. Nevertheless it is possible to retrieve information on cloud structure and thermodynamic cloud phase. In the following subsections, we use cases B and D to discuss the capabilities and limits of lidar under the influence of multiple scattering.

4.1 Cloud structure

At least cloud top or cloud base of a cloud system can be determined straightforward from lidar observations depending on the viewing direction of the lidar. In the case of airborne nadir measurements, the cloud top of boundary layer clouds additionally provides an indication of the height of the planetary boundary layer. If the lidar signal is not attenuated completely, the cloud base can be observed. This is practicable for optically thick clouds with an optical depth up to 3 (You et al., 2006) in the case of homogeneous cloud systems, and up to an optical depth around 15 for clouds with small local inhomogeneities (case B). The usually very high backscattering of liquid water clouds produces an enhanced signal from the whole cloud range to the other cloud boundary. However, in this case, no quantitative analysis of the lidar profile and therefore calculation of the optical thickness can be performed. As criterion if the second boundary was reliable, we analyzed if further cloud structures or the ground return were visible through an optically thick cloud.

ACPD
9, 15125–15179, 2009

In case B, a relatively homogeneous boundary layer cloud with high optical depth (around 13 to 17, estimated from albedometer measurements, see Sect. 2.4.2) was observed. Despite the large values of the optical depth, the ground return of the open ocean was visible, possibly due to small-scale inhomogeneities of the clouds. This reveals that the laser pulses penetrated the clouds. Between the cloud top and the surface, structures with high backscattering ratio were detected by the lidar signal. For this cloud, layers of liquid water were identified at cloud top. As the uppermost layer of a cloud has the highest influence on radiative transfer modeling (Ehrlich et al., 2009), it is crucial to determine the geometrical depth of this layer. Lidar measurements provide this information by defining the liquid cloud layer as the height interval with high backscattering ratio (here, the threshold backscatter ratio was chosen arbitrarily as 30).

In case B, liquid water was found at altitudes between 900 and 1600 m. The mean geometrical thickness of the water layer was estimated with 280(±80) m for the relatively homogeneous cloud. This is in agreement with in situ measurements (see Gayet et al., 2009). At the altitude between 800 and 1500 m the in situ measurements detected liquid water droplets (not shown, see Gayet et al., 2009). For single profiles, the water layer geometrical depth ranged from 100 to 700 m. The values cannot be compared directly with the AMALi observations due to the time delay and advection. However, the spatial characteristics of the liquid water layer observed by in situ measurements are in agreement with the vertical extent of the liquid cloud layer from the airborne lidar measurements.

Also in the airborne zenith measurements of case D, the lidar pulses penetrated the double layer structure. The cirrus cloud above was also detected, thus the observed cloud boundaries are reliable despite multiple scattering effects.

4.2 Validation of lidar cloud phase

For cases B and D the depolarization signal was analyzed to identify the cloud thermodynamic phase.

The depolarization values of about 10% observed for cloud system B are typical for

ACPD
9, 15125–15179, 2009

optically thick liquid water clouds in which multiple scattering occurs, as shown by the detailed analysis of the lidar profiles in Sect. 3.3. This indication of a cloud top layer dominated by liquid water droplets is consistent with the observations of glory from the aircraft (see Rauber and Tokay, 1991; Ehrlich et al., 2009). In the mixing zone of the air masses the cloud was completely glaciated, as confirmed by the ice index calculations. The values of the in situ measurements cannot be compared directly with the AMALi observations due to the time delay and advection. However, the spatial characteristics of the liquid water layer observed by in situ measurements are in agreement with the vertical extent of the liquid cloud layer from the airborne lidar measurements.

For the measurements of case D, the cloud phase of the double layer cloud was determined from the profiles of backscatter and depolarization ratio. In the time series of the backscatter ratio (Fig. 12), the areas of enhanced backscatter ratio are encircled in black. The depolarization values for these cloud parts are depleted (Fig. 13). The analysis of single profiles of backscatter and depolarization ratio (Fig. 15) provides further evidence of two geometrically small liquid water clouds with an ice layer below each liquid cloud layer. The gradual increase of the depolarization signal in the highly backscattering height intervals is caused by multiple scattering, whereas the prompt increase of the depolarization signal in the layers below the liquid clouds is interpreted as the existence of depolarizing ice crystals.

5 Outlook: Importance of lidar for atmospheric studies

Elastic lidar systems provide reliable information on vertical cloud structures in high spatial and temporal resolution. The basic information about cloud altitude is essential for understanding cloud formation and evolution processes as well as for radiative transfer studies (Shupe and Intrieri, 2004) and climate modeling (Inoue et al., 2006). Other data about the vertical dimension of clouds are provided by e.g. radio sondes or airborne in situ measurements. These instruments either give a only a single vertical profile of the meteorological parameters (radio sonde) or have to probe different cloud

ACPD
9, 15125–15179, 2009

altitudes consecutively (in situ instruments). Radar also provides vertical cloud profiles. In comparison with lidar, even radar systems of a relatively short wavelength (e.g. 8.66 mm) are more sensitive to large ice crystals and typically have a lower vertical resolution (Intrieri et al., 2002a).

Our observations (case A) and of Lampert et al. (2009) demonstrate that subvisible clouds occur at least occasionally in the Arctic. As they show up in lidar systems they cannot be neglected for radiative transfer calculations. Little is known about the frequency of occurrence of these subvisible clouds and their radiative impact in the Arctic. However, the study of Wyser et al. (2008) suggests the existence of many optically thin clouds in winter. The observation of a cloud consisting of sub-µm liquid pre-condensed particles at low temperatures (−30°C) might be of importance for radiative transfer calculations and climate modeling. For future campaigns it is recommended to analyze the formation process and life time of such optically thin supercooled pre-condensation layers and compare the lidar observations with the microphysics data obtained by in situ instruments.

Cloud phase plays a crucial role for the surface energy budget (McFarquhar and Cober, 2004).

With depolarization lidar, the thermodynamic phase of the cloud layer closest to the lidar system was retrieved even under conditions of multiple scattering (cases B and D).

The precise estimation of a LR from remote sensing data provides valuable information about internal processes in clouds (e.g. the growth/shrinking of small-size cloud particles). Lampert et al. (2009) estimated the LR of an Arctic ice clouds from in situ and remote sensing information, yielding a result of 20 sr. Here we presented an example of an ice cloud with a highly variable internal structure (case C). The observation of ice cloud layers with very different optical properties seems a special case compared to the microphysical findings of Korolev et al. (2000) and Bailey and Hallett (2002), who describe prevailing irregular structures of ice crystals for a wide temperature range. A high backscatter peak for the 355 nm wavelength, resulting in a low LR was found.

ACPD
9, 15125–15179, 2009

Our observations underline that even in a pristine Arctic environment without anthropogenic pollution, ice clouds cannot be considered as a homogeneous, simple phenomenon. This might pose a challenge for the precise description of pure ice clouds in climate models.

This study demonstrates that lidar observations provide an indispensable complement to other instruments for atmospheric studies. They deliver information about cloud structure, cloud phase, optical properties and rough estimates of microphysical properties in high temporal and spatial resolution. However, only closure experiments with a combination of in situ instrumentation and radiation sensors will yield a complete understanding of Arctic clouds.

Acknowledgements. We would like to thank the DLR flight crew and the OPTIMARE GmbH for their support with the airborne measurements, and the AWIPEV base personnel for the measurements and attendance of the instruments in Ny-Ålesund. The MPLNET project is funded by the NASA Earth Observing System and Atmospheric Radiation Sciences Program.

References

Ackermann, J.: The extinction-to-backscatter ratio of tropospheric aerosol: A numerical study, J. Atmos. Oceanic. Technol., 15, 1043–1050, 1998.

d'Almeida, G. A., Koepke, P., and Shettle, E. P.: Atmospheric Aerosols: Global Climatology and Radiative Characteristics, A. Deepak Publishing, Hampton, VA, ISBN 0-937194-22-0, 1991.

Ansmann, A., Wandinger, U., Riebesell, M., Weitkamp, C., and Michaelis, W.: Independent measurement of extinction and backscatter profiles in cirrus clouds by using a combined Raman elastic-backscatter lidar, Appl. Opt. 31, 7113–7113, 1992.

Bailey, M. and Hallett, J.: Nucleation effects on the habit of vapour grown ice crystals from −18 to −42°C, Q. J. Roy. Meteor. Soc., 128, 1461–1483, 2002.

Bissonnette, L. R., Roy, G., and Roy, N.: Multiple-scattering-based lidar retrieval: method and results of cloud probings, Appl. Opt., 44(26), 5565–5581, 2005.

Böckmann, C.: Hybrid regularization method for the ill-posed inversion of multiwavelength lidar data to determine aerosol size distribution, Appl. Opt., 40, 1329–1342, 2001.

Boudala, F. S., Isaac, G. A., Cober, S. G., and Fu, Q.: Liquid fraction in stratiform mixed- phase clouds from in situ observations, Quart. J. Roy. Meteor. Soc., 130, 2919–2931, 2004.

Campbell, J. R. and Shiobara, M.: Glaciation of a mixed-phase boundary layer cloud at a coastal arctic site as depicted in continuous lidar measurements, Polar Science, 2, 121–127, 2008.
Chen, W. N., Chiang, C. W., and Nee, J. B.: Lidar ratio and depolarisation ratio for cirrus clouds, Appl. Optics, 31, 6470–6476, 2002.
Chen, C. C., Hakim, G. J., and Durran, D. R.: Transient mountain waves and their interaction with large scales, J. Atmos. Sci., 64, 7, 2378–2400, 2007.
Christensen, J. H., Christensen, O. B., Lopez, P., van Mijgaard, E., and Botzet, M.: The HIRHAM4 regional atmospheric climate model, DMI Science Rep. 96-4, 1–51, 1996.
Collins, W. D., Bitz, C. M., Blackmon, M. L., Bonan, G. B., Bretherton, C. S., Carton, J. A., Chang, P., Doney, S. C., Hack, J. J., Henderson, T. B., Kiehl, J. T., Large, W. G., McKenna, D. S., Santer, B. D., and Smith, R. D.: The Community Climate System Model: CCSM3, J. Climate, 19, 2122–2143, 2006.
Curry, J. A., Schramm, J. L., and Ebert, E. E.:, Impact of Clouds on the Surface Radiation Balance of the Arctic Ocean, Meteorol. Atmos. Phys. 51, 197–217, 1993.
Curry, J. A., Rossow, W. B., Randall, D., and Schramm, J. L.: Overview of Arctic Cloud and Radiation Characteristics, J. Climate, 9, 1731–1764, 1996.
Curry, J. A., Pinto, J. O., Benner, T., and Tschudi, M.: Evolution of the cloudy boundary layer during the autumnal freezing of the Beaufort Sea, J. Geophys. Res., 102(D12), 13851–13860, 1997.
Curry, J. A., Hobbs, P. V., King, M. D., Randall, D. A., Minnis, P., Isaac, G. A., Pinto, J. O., Uttal, T., Bucholtz, A., Cripe, D. G., Gerber, H., Fairall, C. W., Garrett, T. J., Hudson, J., Intrieri, J. M., Jakob, C., Jensen, T., Lawson, P., Marcotte, D., Nguyen, L., Pilewskie, P., Rangno, A., Rogers, D. C., Strawbridge, K. B., Valero, F. P. J., Williams, A. G., and Wylie, D.: FIRE Arctic clouds experiment, B. Am. Meteorol. Soc., 81, 1, 5–29, 2000.
Draxler, R. R. and Hess, G. D.: An overview of the Hysplit_4 modeling system for trajectories, dispersion, and deposition, Aust. Met. Mag., 47, 295–308, 1998.
Dye, J. E. and Baumgardner, D.: Evaluation of the forward scattering spectrometer probe. part I: Electronic and optical studies, J. Atmos. Oceanic Technol., 1, 329–344, 1984.
Ehrlich, A., Bierwirth, E., Wendisch, M., Gayet, J.-F., Mioche, G., Lampert, A., and Heintzenberg, J.: Cloud phase identification of Arctic boundary-layer clouds from airborne spectral reflection measurements: test of three approaches, Atmos. Chem. Phys., 8, 7493–7505, 2008,

http://www.atmos-chem-phys.net/8/7493/2008/.
Ehrlich, A., Wendisch, M., Bierwirth, E., Gayet, J.-F., Mioche, G., Lampert, A., and Mayer, B.: Evidence of ice crystals at cloud top of Arctic boundary-layer mixed-phase clouds derived from airborne remote sensing, Atmos. Chem. Phys. Discuss., 9, 13801–13842, 2009, http://www.atmos-chem-phys-discuss.net/9/13801/2009/.
Ehrlich, A.: The Impact of Ice Crystals on Radiative Forcing and Remote Sensing of Arctic Boundary-Layer Mixed-Phase Clouds, PhD thesis, http://ubm.opus.hbz-nrw.de/frontdoor.php?source_opus=2001, 2009.
Gayet, J.-F., Crépel, O., Fournol, J. F., and Oshchepkov, S.: A new airborne polar nephelometer for the measurements of optical and microphysical cloud properties. Part I: Theoretical design, Ann. Geophys., 15, 451–459, 1997, http://www.ann-geophys.net/15/451/1997/.
Gayet, J.-F., Stachlewska, I. S., Jourdan, O., Shcherbakov, V., Schwarzenboeck, A., and Neuber, R.: Microphysical and optical properties of precipitating drizzle and ice particles obtained from alternated lidar and in situ measurements, Ann. Geophys., 25, 1487–1497, 2007, http://www.ann-geophys.net/25/1487/2007/.
Gayet, J.-F., Mioche, G., Drnbrack, A., Ehrlich, A., Lampert, A., and Wendisch, M.: Microphysical and optical properties of Arctic mixed-phase clouds – the 9 April 2007 case study, Atmos. Chem. Phys. Discuss., 9, 11333–11366, 2009, http://www.atmos-chem-phys-discuss.net/9/11333/2009/.
Giannakaki, E., Balis, D. S., Amiridis, V., and Kazadzis, S.: Optical and geometrical characteristics of cirrus clouds over a Southern European lidar station, Atmos. Chem. Phys., 7, 5519–5530, 2007, http://www.atmos-chem-phys.net/7/5519/2007/.
Haag, W. and Kärcher, B.: The impact of aerosol and gravity waves on cirrus clouds in midlatiudes, J. Geophys. Res., 109, D12202, doi:10.1029/2004JD004579, 2004.
Harrington, J. Y., Reisin, T., Cotton, W. R., and Kreidenweis, S. M.: Cloud resolving simulations of Arctic stratus, part II: Transition-season clouds, Atmos. Res., 51, 45–75, 1999.
Herber, A., Thomason, L. W., Gernandt, H., Leiterer, U., Nagel, D., Schulz, K.-H., Kaptur, J., Albrecht, T., and Notholt, J.: Continuous day and night aerosol optical depths observations in the Arctic between 1991 and 1999, J. Geophys Res. 107(D10), 4097, doi:10.1029/2001JD000536, 2002.
Hobbs, P. V., Rangno, A. L., Shupe, M., and Uttal, T.: Airborne studies of cloud structures over

the Arctic Ocean and comparison with retrievals from ship-based remote sensing measurements, J. Geophys. Res., 106(D14), 15029–15044, 2001.
Hoffmann, A., Ritter, C., Stock, M., and Shiobara, M.: Ground-based lidar measurements from Ny-Ålesund during ASTAR 2007: a statistical overview, in preparation for Atmos. Chem. Phys. Discuss., submitted, 2009.
Hu, Y., Winker, D., Yang, P., Baum, B., Poole, L., and Vann, L.: Identification of cloud phase from PICASSO-CENA lidar depolarization: a multiple scattering sensitivity study, J. Quant. Spectrosc. Ra., 70, 569–579, 2001.
Hu, Y., Liu, Z., Winker, D., Vaughan, M., and Noel, V.: Simple relation between lidar multiple scattering and depolarization for water clouds, Opt. Lett., 31, 12, 1809–1811, 2006.
Hu, Y., Vaughan, M., Liu, Z., Lin, B., Yang, P., Flittner, D., Hunt, B., Kuehn, R., Huang, J., Wu, D., Rodier, S., Powell, K., Trepte, C., and Winker, D.: The depolarization – attenuated backscatter relation: CALIPSO lidar measurements vs. theory, Opt. Express, 15(9), 5327–5332, 2007.
IPCC: Climate Change 2007: The Physical Science Basis. Contribution of Working Group I to the Fourth Assessment Report of the Intergovernmental Panel on Climate Change, edited by: Solomon, S., Qin, D., Manning, M., Chen, Z., Marquis, Z. M., Averyt, K. B., Tignor M., and Miller, H. L., Cambridge University Press, 996 pp., 2007.
Inoue, J., Liu, J., Pinto, J. O., and Curry, J. A.: Intercomparison of Arctic Regional Climate Models: Modeling Clouds and Radiation for SHEBA in May 1998, J. Climate, 19, 4167–4178, 2006.
Intrieri, J. M., Shupe, M. D., Uttal, T., and McCarty, B. J.: An annual cycle of Arctic cloud characteristics observed by radar and lidar at SHEBA, J. Geophys. Res., 107(C10), 8030, doi:10.1029/2000JC000423, 2002a.
Intrieri, J. M., Fairall, C. W., Shupe, M. D., Persson, P. O. G., Andreas, E. L., Guest, P. S., and Moritz, R. E.: An annual cycle of Arctic surface cloud forcing at SHEBA, J. Geophys. Res., 107(C10), 8039, doi:10.1029/2000JC000439, 2002b.
Ishii, S., Shibata, T., Nagai, T., Mizutani, K., Itabe, T., Hirota, M., Fujimoto, T., and Uchino, O.: Arctic haze and clouds observed by lidar during four winter seasons of 1993–1997, at Eureka, Canada, Atmos. Environ., 33, 2459–2470, 1999.
Jiang, H., Cotton, W. R., Pinto, J. O., Curry, J. A., and Weissbluth, M. J: Cloud resolving simulations of mixed-phase Arctic stratus observed during BASE: Sensitivity to concentration of ice crystals and large-scale heat and moisture advection, J. Atmos. Sci., 57, 2105–2117,

ACPD
9, 15125–15179, 2009

2000.
Jourdan, O., Oshchepkov, S., Shcherbakov, V., Gayet, J.-F., and Isaka, H.: Assessment of cloud optical parameters in the solar region: Retrievals from airborne measurements of scattering phase functions, J. Geophys. Res., 108(D18), 4572, doi:10.1029/2003JD003493, 2003.
Key, J. R. and Intrieri, J. M.: Cloud Particle Phase Determination with the AVHRR, J. Appl., Met., 39, 1797–1804, 2000.
Key, E. L., Minnett, P. J., and Jones, R. A.: Cloud distributions over the coastal Arctic Ocean: surface-based and satellite observations, Atmos. Res., 72, 57–88, 2004.
Klett, J. D.: Lidar inversions with variable backscatter/extinction values, Appl. Opt., 24, 1638–1648, 1985.
Kirsche, A.: Regularisierungsverfahren: Entwicklung, Konvergenzuntersuchung und optimale Anpassung für die Fernerkundung, PhD thesis, University Potsdam, 2008.
Kirsche, A. and Böckmann, C.: Pade iteration method for regularization, Appl. Math. Comput., 180, 648–663, 2006.
Komppula, M., Lihavainen, H., Kerminen, V.-M., Kulmala, M., and Viisanen, Y.: Measurements of cloud droplet activation of aerosol particles at a clean subarctic background site, J. Geophys. Res., 110, D06204, doi:10.1029/2004JD005200, 2005.
Korhonen, P., Kulmala, M., Hansson, H.-C., Svenningsson, I. B., and Rusko, N.: Hygroscopicity of pre-existing particle distribution and formation of cloud droplets: A model study, Atmos. Res., 41, 249–266, 1996.
Korolev, A., Isaac, G. A., and Hallett, J.: Ice particle habits in stratiform clouds, Q. J. Roy. Meteor. Soc., 126, 2873–2902, 2000.
Korolev, A. and Isaac, G.: Phase transformation of mixed-phase clouds, Q. J. Roy. Meteor. Soc., 129, 19–38, 2003.
Korolev, A. V., Isaac, G. A., Cober, S. G., Strapp, J. W., and Hallett, J.: Microphysical characterization of mixed-phase clouds, Q. J. Roy. Meteor. Soc., 129, 39–65, 2003.
Korolev, A. and Field, P. R.: The effect of dynamics on mixed-phase clouds: Theoretical considerations, J. Atmos. Sci., 65, 66–86, 2008.
Kupfer, H., Herber, A., and König-Langlo, G.: Radiation measurements and synoptic observations at Ny-Ålesund, Reports on Polar Research, 538, 75, http://epic.awi.de/Publications/Kup2006a.pdf, 2006.
Lampert, A., Ehrlich, A., Drnbrack, A., Jourdan, O., Gayet, J.-F., Mioche, G., Shcherbakov, V., Ritter, C., and Wendisch, M.: Microphysical and radiative characterization of a subvisible

midlevel Arctic ice cloud by airborne observations – a case study, Atmos. Chem. Phys., 9, 2647–2661, 2009, http://www.atmos-chem-phys.net/9/2647/2009/.

Law, K. S., Ancellet, G., Pelon, J., Turquety, S., Clerbaux, C., Pommier, M., de Villiers, R., Gayet, J.-F., Schwarzeboeck, A., Nedelec, P., Schneider, J., and Borrmann, S.: POLARCAT-France Airborne Experiment: first results. /Intern. Global Atmospheric Chemistry conference (IGAC)/, 7–12 September 2008, Annecy, France, 2008.

Lawson, P., Heymsfield, A. J., Aulenbach, S. M., and Jensen, T. L.: Shapes, sizes and light scattering properties of ice crystals in cirrus and a persistent contrail during SUCCES, Geophys. Res. Lett., 25, 1331–1334, 1998.

Lawson, R. P., Baker, B. A., and Schmitt, C. G.: An overview of microphysical properties of Arctic clouds observed in May and July 1998 during FIRE ACE, J. Geophys. Res., D14, 14989–15014, 2001.

Luo, Y., Xu, K.-M., Morrison, H., McFarquhar, G. M., Wang, Z., and Zhang, G.: Multilayer arctic mixed-phase clouds simulated by a cloud-resolving model: Comparison with ARM observations and sensitivity experiments, J. Geophys. Res., 113, D12208, doi:10.1029/2007JD009563, 2008.

McFarquhar, G. M. and Cober, S. G.: Single scattering properties of mixed phase Arctic clouds at solar wavelengths: Impact on radiative transfer, J. Climate, 17, 19, 3799–3813, 2004.

McFarquhar, G. M., Zhang, G., Poellot, M. R., Kok, G. L., McCoy, R., Tooman, T., Fridlind, A., and Heymsfield, A. J.: Ice properties of single-layer stratocumulus during the mixed-phase Arctic cloud experiment: 1. observations, J. Geophys. Res., 112, D24201, doi:10.1029/2007JD008633, 2007.

Morrison, H., Pinto, J. O., Curry, J. A., and McFarquhar, G. M.: Sensitivity of modeled Arctic mixed-phase stratocumulus to cloud condensation and ice nuclei over regionally varying surface conditions, J. Geophys. Res., 113, D05203, doi:10.1029/2007JD008729, 2008.

Nakajima, T. and King, M.: Determination of the optical thickness and effective particle radius of clouds from reflected solar radiation measurements. Part I: Theory, J. Atmos. Sci., 47, 1878–1893, 1990.

Nicolas, F., Bissonnette, L. R., and Flamant, P. H.: Lidar effective multiple-scattering coefficients in cirrus clouds, Appl. Opt., 36(15), 3458–3468, 1997.

Oshchepkov, S. L., Isaka. H., Gayet, J. F., Sinyuk, A., Auriol, F., and Havemann, S.: Microphysical properties of mixed-phase & ice clouds retrieved from in situ airborne “Polar Nephelome-

ter" measurements, Geophys. Res. Lett., 27, 209–213, 2000.
Pinto, J.: Autumnal Mixed-Phase Cloudy Boundary Layers in the Arctic, J. Atmos. Sci., 55, 2016–2037, 1998.
Pinto, J. O., Curry, J. A., and Intrieri, J. M.: Cloud-aerosol interactions during autumn over Beaufort Sea, J. Geophys. Res., 106(D14), 15077–15097, 2001.
Pornsawad, P., Böckmann, C., Ritter, C., and Rafler, M.: Ill-posed retrieval of aerosol extinction coefficient profiles from Raman lidar data by regularization, Appl. Optics 47, 1649–1661, 2008.
Rauber, R. M. and Tokay, A.: An explanation for the existence of supercooled water at the top of cold clouds, J. Atmos. Sci., 48(8), 1005–1023, 1991.
Reichardt, J., Reichardt, S., Hess, M., and McGee, T. J.: Correlations among the optical properties of cirrus-cloud particles: Microphysical interpretation, J. Geophys. Res., 107(D21), 4562, doi:10.1029/2002JD002589, 2002.
Richter, A., Gayet, J.-F., Mioche, G., Ehrlich, A., and Dörnbrack, A.: Mixed-Phase Clouds in the Arctic: A Synopsis of Airborne Lidar, In-Situ, and Albedometer Observations, complemented by Meteorological Analyses. 24th International Laser Radar Conference (ILRC), 23–27 June 2008, Boulder, USA, 881–884, 2008.
Ritter, C., Kirsche, A., and Neuber, R.: Tropospheric Aerosol characterized by a Raman Lidar over Spitsbergen, Proceedings of the 22nd International Laser Radar Conference (ILRC2004), ESA SP-561, 459–462, 2004.
Sandvik, A., Biryulina, M., Kvamstø, N. G., Stamnes J. J., and Stamnes, K.: Observed and simulated composition of Arctic clouds: Data properties and model validation, J. Geophys. Res., 112, D05205, doi:10.1029/2006JD007351, 2007.
Sassen, K., Griffin, M. K., and Dodd, G. C.: Optical Scattering and microphysical properties of subvisual cirrus clouds, and climatic implications, J. Appl. Meteorol., 28, 91–98, 1989.
Sassen, K. and Comstock, J.: A midlatitude cirrus cloud climatology from the facility for atmospheric remote sensing. part III: radiative properties, J. Atmos. Sci., 58, 2113–2127, 2001.
Scheuer, E., Talbot, R. W., Dibb, J. E., Seid, G. K., and DeBell, L.: Seasonal distributions of fine aerosol sulfate in the North American Arctic basin during TOPSE, J. Geophys. Res. 108(D4), 8370, doi:10.1029/2001JD001364, 2003.
Shiobara, M., Yabuki, M., and Kobayashi, H.: A polar cloud analysis based on micro-pulse lidar measurements at Ny-Alesund, Svalbard and Syowa, Antarctica, Phys. Chem. Earth, 28, 1205–1212, 2003.

Shupe, M. D. and Intrieri, J. M.: Cloud radiative forcing of the Arctic surface: The influence of cloud properties, surface albedo and solar zenith angle, J. Climate, 17, 616–628, 2004.
Shupe, M. D., Kollias, P., Persson, P. O. G., and McFarquhar, G. M.: Vertical motions in arctic mixed-phase stratiform clouds, J. Atmos. Sci., 65, 1304–1322, 2008.
Spinhirne, J. D.: Micro pulse lidar, IEEE Trans. Geosci. Remote Sens., 31, 48–55, 1993.
Stachlewska, I. S., Wehrle, G., Stein, B., and Neuber, R.: Airborne Mobile Aerosol Lidar for measurements of Arctic aerosols, Proceedings of the 22nd International Laser Radar Conference (ILRC2004), ESA SP-561, 1, 87–89, 2004.
Stachlewska, I. S., Neuber, R., Lampert, A., and Ritter, C.: AMALi – the Airborne Mobile Aerosol Lidar for Arctic research, Atmos. Chem. Phys. Discuss., submitted, 2009.
Stohl, A.: Characteristics of atmospheric transport into the Arctic troposphere, J. Geophys. Res, 111, D11306, doi:10.1029/2005JD006888, 2006.
Ström, J., Umegård, J., Tørseth, K., Tunved, P., Hansson, H.-C., Holmén, K., Wismann, V., Herber, A., and König-Langlo, G.: One year of particle size distribution and aerosol chemical composition measurements at the Zeppelin Station, Svalbard, March 2000–March 2001, Phys. Chem. Earth, 28, 1181–1190, 2003.
Tomasi, C. and Tampieri, F.: Size distribution models of small water droplets in mist and their volume extinction coefficients at visible and infrared wavelengths, Atmos. Environ., 10, 1005–1013, 1976.
Turner, D. D.: Arctic mixed-phase cloud properties from AERI lidar observations: Algorithm and results from SHEBA, J. Appl. Meteo., 44, 427–444, 2005.
Vavrus, S.: The impact of cloud feedbacks on Arctic climate under greenhouse forcing, J. Climate, 17(3), 603–615, 2004.
Verlinde, J., Harriongton, J. Y., McFarquhar, G. M., et al.: The Mixed-Phase Arctic Cloud Experiment (M-PACE), B. Am. Meteorol. Soc., 88, 205–221, 2007.
Welton, E. J., Campbell, J. R., Spinhirne, J. D., and Scott, V. S.: Global monitoring of clouds and aerosols using a network of micro-pulse lidar systems, Proc. Int. Soc. Opt. Eng., 4153, 151–158, 2001.
Wendisch, M., Müller, D., Schell, D., and Heintzenberg, J.: An airborne spectral albedometer with active horizontal stabilization, J. Atmos. Oceanic Technol., 18, 1856–1866, 2001.
Wyser, K., Jones, C. G., Du, P., Girard, E., Willén, U., Cassano, J., Christensen, J. H., Curry, J. A., Dethloff, K., Haugen, J.-E., Jacob, D., Køltzow, M., Laprise, R., Lynch, A., Pfeifer, S., Rinke, A., Serreze, M., Shaw, M. J., Tjernström, M., and Zagar, M.: An evaluation of

Arctic cloud and radiation processes during the SHEBA year: Simulation results from eight Arctic regional climate models, Clim. Dynam., 30, 203–223, doi:10.1007/s00382-007-0286-1, 2008.

You, Y., Kattawar, G. W., Yang, P., Hu, Y. X., and Baum, B. A.: Sensitivity of depolarized lidar signals to cloud and aerosol particle properties, J. Quant. Spectrosc. Ra., 100, 470–482, 2006.

Table 1. Technical specifications of the three lidar systems and resolution of the data used for this study.

	MPL	KARL	AMALi
Laser	Nd:YLF	Nd:YAG	Nd:YAG
Emitted wavelengths [nm]	523	1064, 532, 355	532, 355
Detected wavelengths [nm]	523	1064, 532, 355 387, 407, 607, 660	532, 355
Telescope diameter [cm]	20	30	10.2
FOV [mrad]	0.10	0.83	3.1
Vertical resolution [m]	30	60	7.5
Time resolution [s]	600	600	15

ACPD
9, 15125–15179, 2009

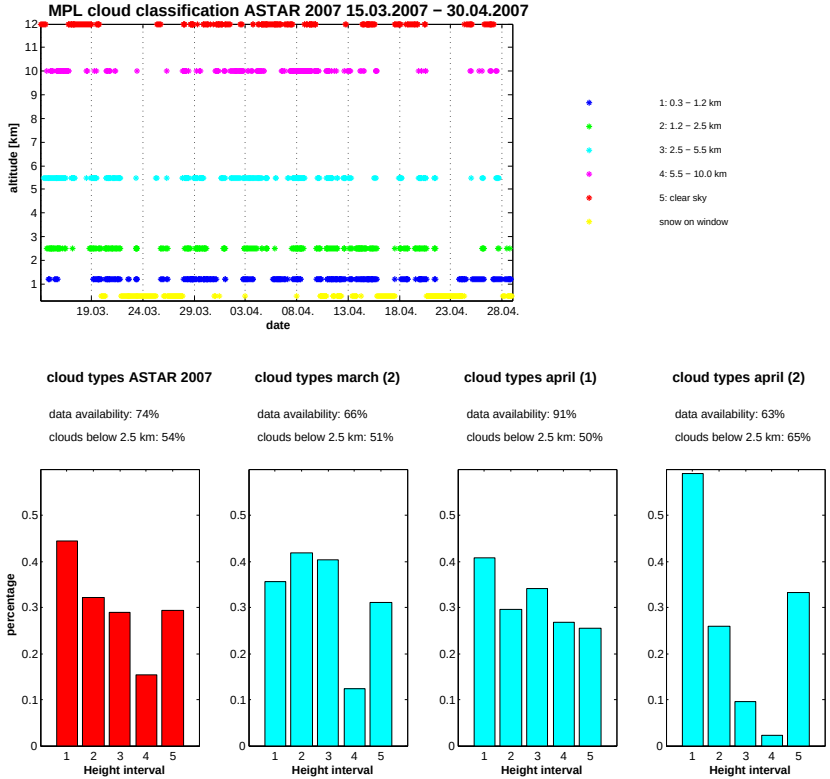

Fig. 1. Top: Occurrence and height distribution of clouds from 15–30 April 2007, observed by MPL. The single observations were classified in 4 height intervals: 0.3–1.2 km (blue), 1.2–2.5 km (green), 2.5–5.5 km (light blue), 5.5–10 km (magenta). Lidar profiles measuring clear sky (red) and snow on the window (yellow) are also indicated.
Bottom: Percentage of cloud cover at different height intervals for the whole time period, and divided into periods of 2 weeks. The percentages refer to the respective time periods with a snow free window. Note that clouds in more than one height interval can be observed simultaneously, thus the percentage values do not add up to unity.

ACPD
9, 15125–15179, 2009

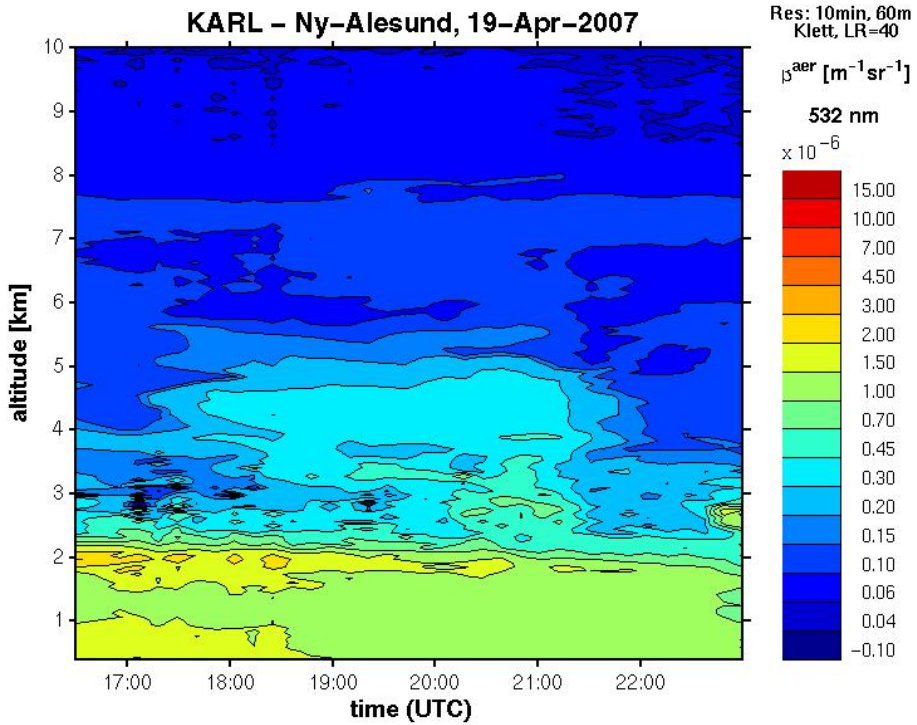

Fig. 2. Time series of the particle backscatter coefficient in Ny-Ålesund on 19 April 2007. The pre-condensation layer (case A) is visible at 2 km altitude.

ACPD
9, 15125–15179, 2009

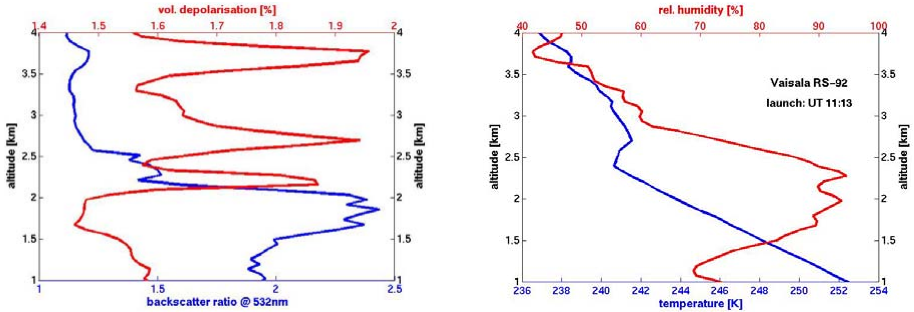

Fig. 3. Profiles of backscatter and depolarization ratio for the height interval of the pre-condensation layer (case A) observed on 19 April 2007 at 16:55 UTC (left), and profiles of temperature and relative humidity measured by the radio sonde launched in Ny-Ålesund on 19 April 2007, 11:13 UTC (right).

ACPD
9, 15125–15179, 2009

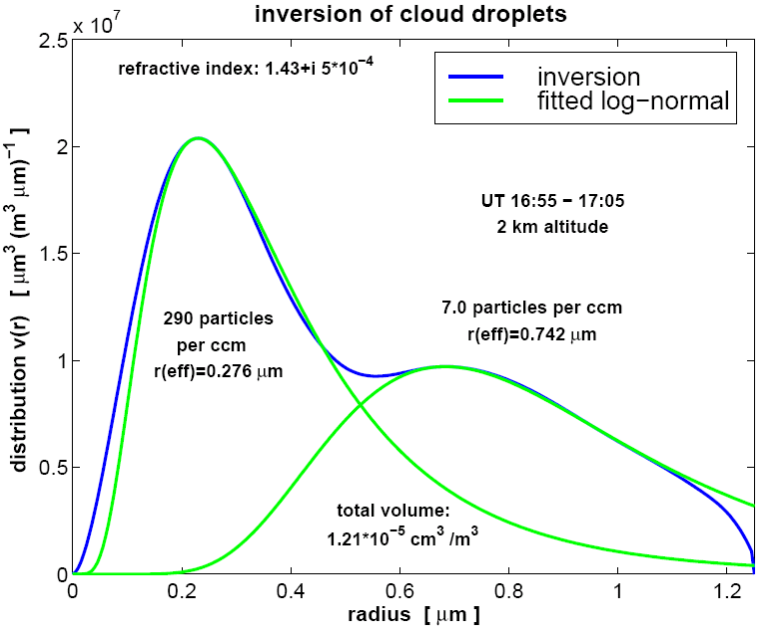

Fig. 4. Microphysical parameters of the pre-condensation layer (case A) on 19 April 2007 at 16:55 UTC, derived from lidar data inversion.

ACPD
9, 15125–15179, 2009

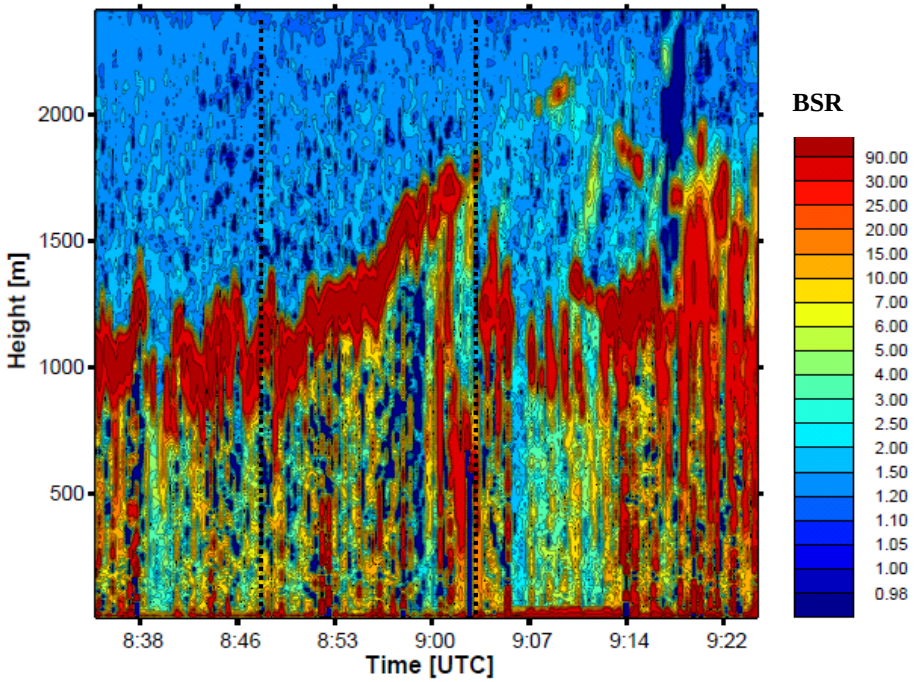

Fig. 5. Time series of airborne lidar backscatter profiles of case B (9 April 2007). The dotted vertical bars indicate the profiles shown in Fig. 7.

ACPD
9, 15125–15179, 2009

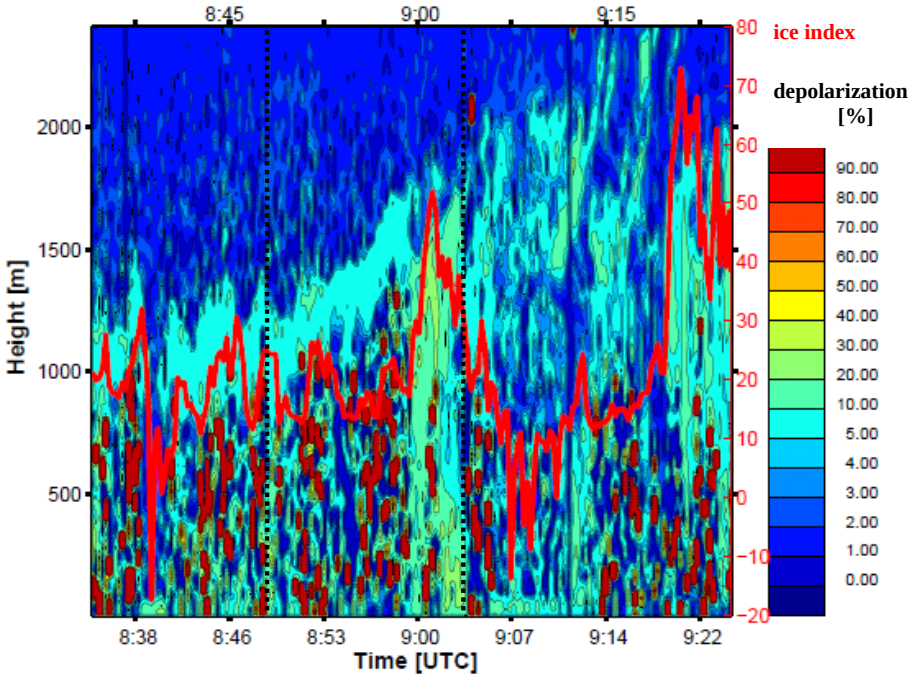

Fig. 6. Time series of airborne lidar depolarization (in %) of case B (9 April 2007). Superimposed in red is the ice index calculated from albedometer observations. The dotted vertical bars indicate the profiles shown in Fig. 7.

ACPD
9, 15125–15179, 2009

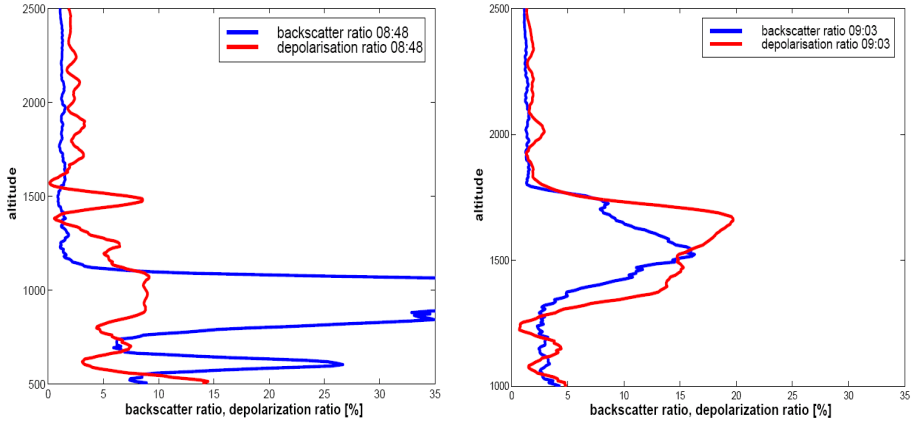

Fig. 7. Profiles of backscattering and depolarization ratios of case B for a liquid-topped cloud at 08:48 UTC (left) and an ice cloud at 09:03 UTC (right) on 9 April 2007.

ACPD
9, 15125–15179, 2009

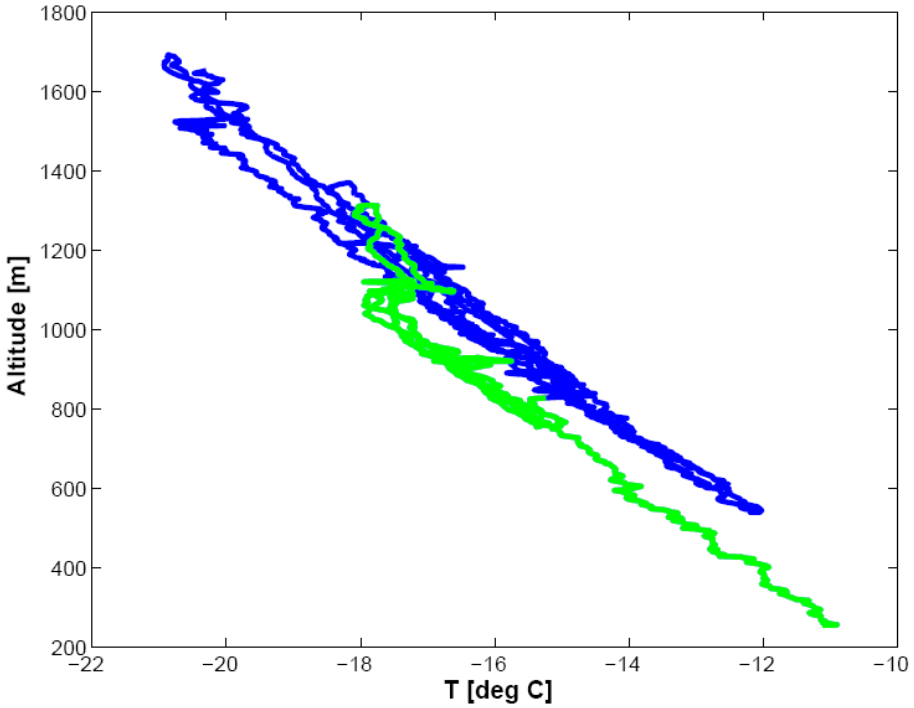

Fig. 8. Temperature profiles measured for case B (9 April 2007). Blue are the profiles measured in the North-West, before 10:18 UTC, and green are the profiles measured in the South-East, after 10:18 UTC. Below the altitude of 1100 m, the air temperature is about 1.5°C colder in the South-East of the flight leg.

ACPD
9, 15125–15179, 2009

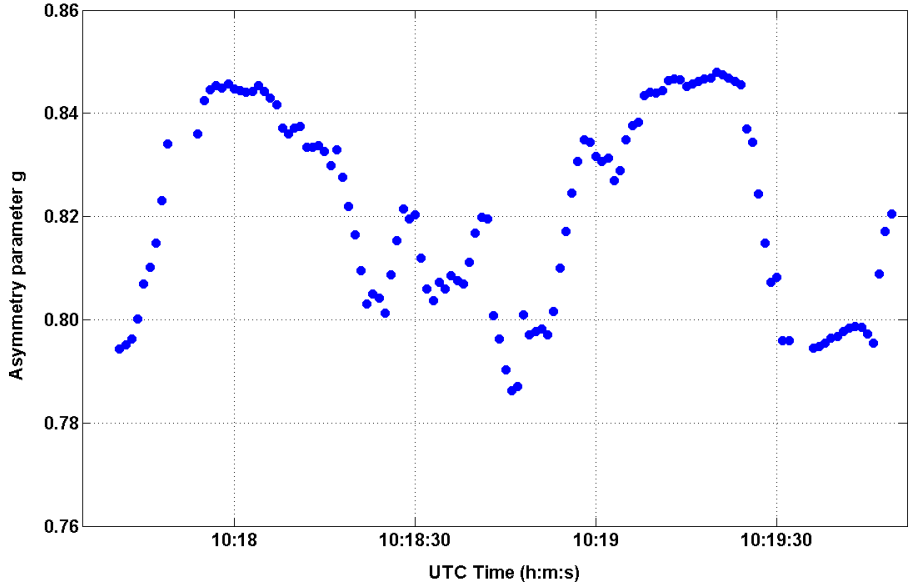

Fig. 9. Time series of the asymmetry parameter in the air mass mixing zone of case B. During 15 s, corresponding to a horizontal extent of around 900 m, only ice was found (g<0.82).

ACPD
9, 15125–15179, 2009

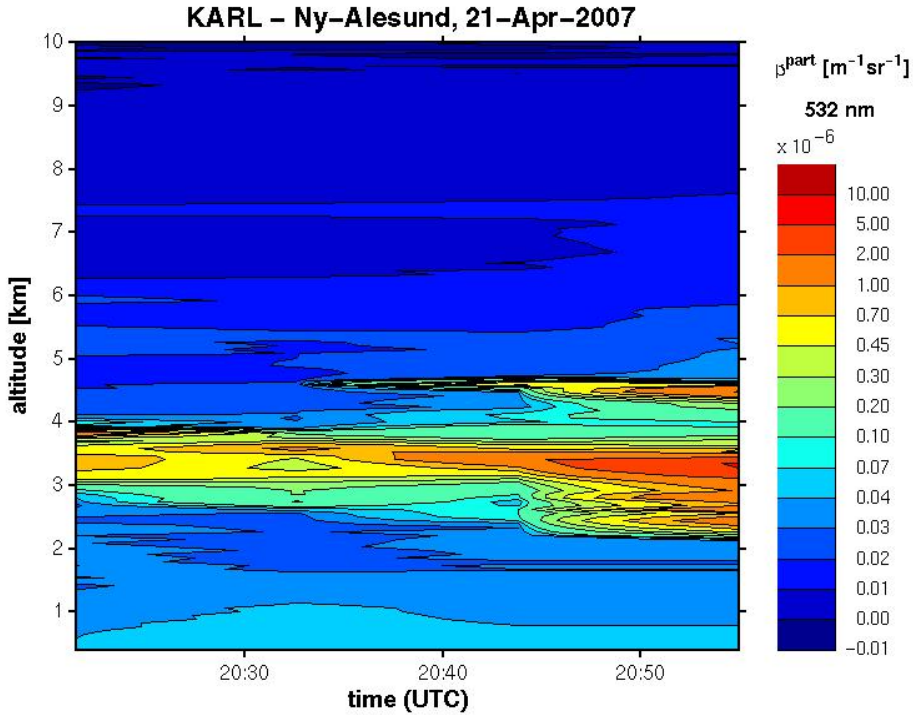

Fig. 10. Time series of the particle backscatter coefficient at Ny-Ålesund of case C (21 April 2007).

ACPD
9, 15125–15179, 2009

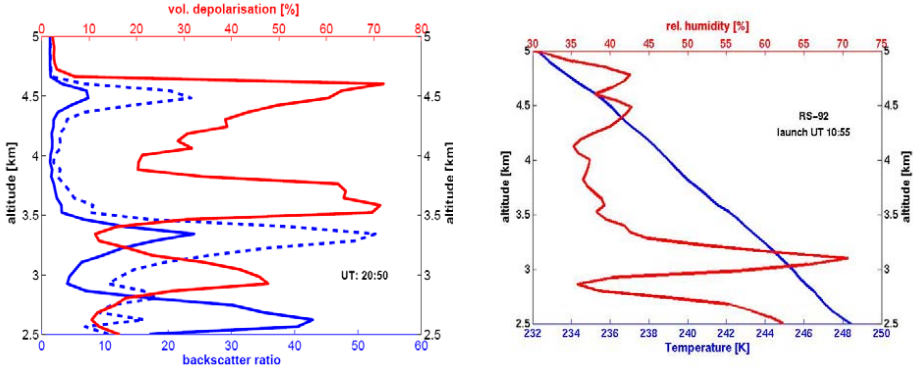

Fig. 11. Left: Backscatter (blue) and depolarization (red) profiles of the cloud observation of case C (21 April 2007) around 20:50 UTC. The dashed blue curve denotes to the backscatter ratio at 532 nm, the blue one to the backscatter ratio at 355 nm. Right: Temperature (blue) and relative humidity (red) profiles of the radio sonde launched at 11:00 UTC on 21 April 2007.

ACPD

9, 15125–15179, 2009

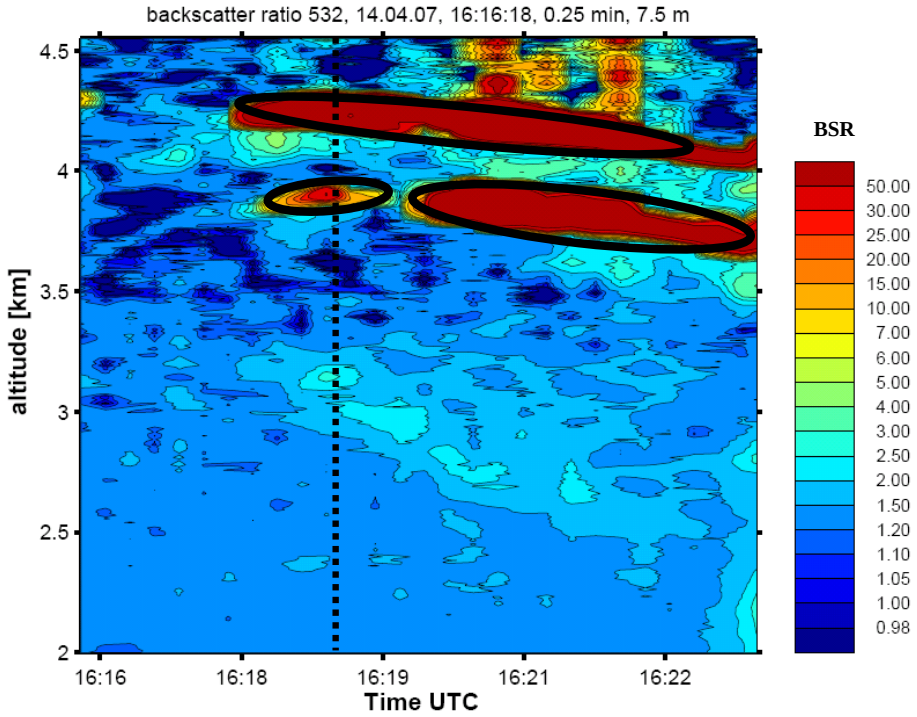

Fig. 12. Time series of the airborne backscattering ratio of case D (14 April 2007). Encircled in black are the cloud areas of high backscatter values. The vertical bar corresponds to the time step of the profile shown in Fig. 15.

ACPD
9, 15125–15179, 2009

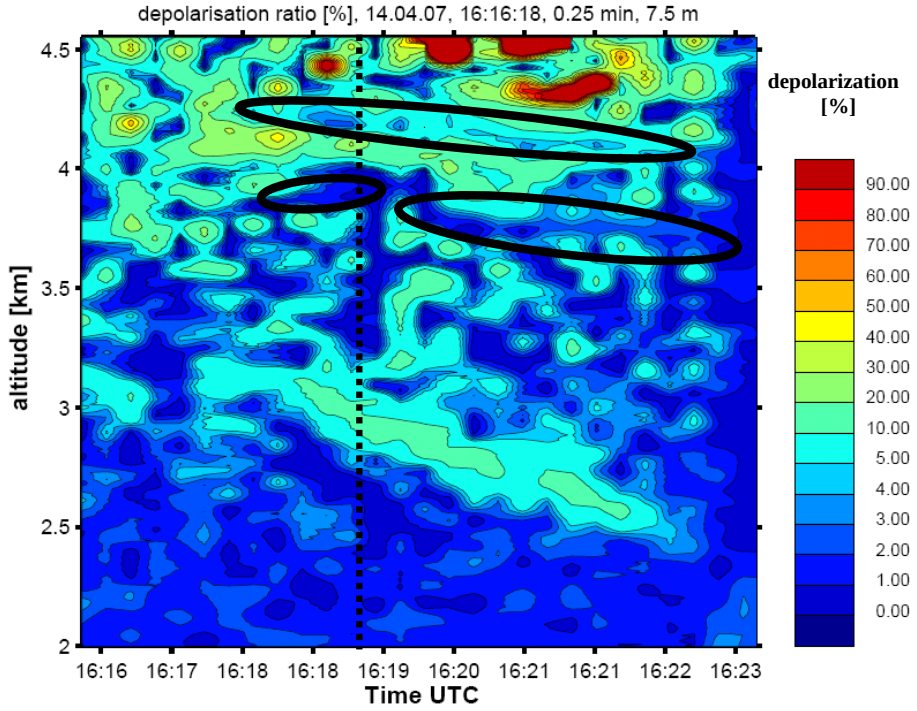

Fig. 13. Time series of the airborne depolarization ratio of case D (14 April 2007). Encircled in black are the same cloud areas as in Fig. 14. The vertical bar corresponds to the time step of the profile shown in Fig. 15.

ACPD
9, 15125–15179, 2009

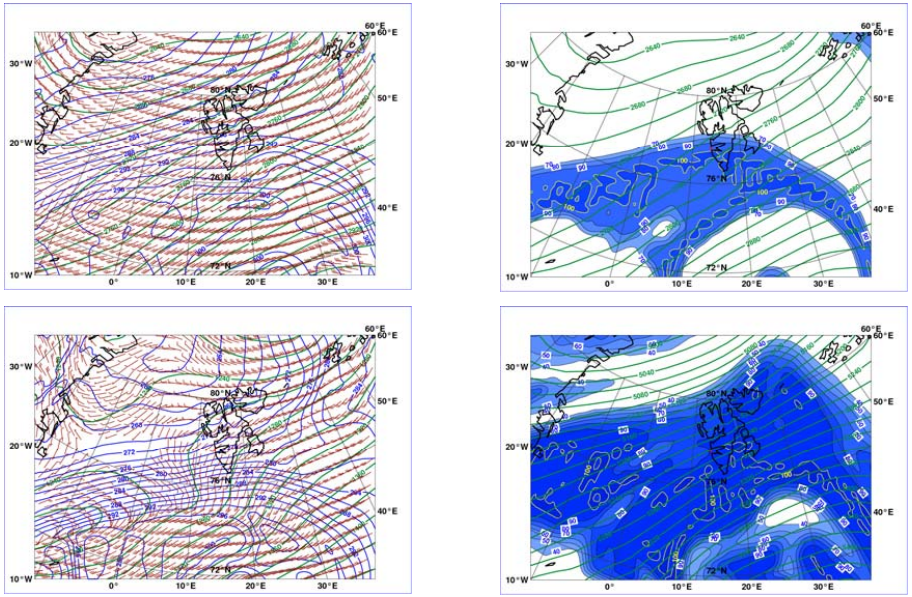

Fig. 14. Left: ECMWF analyses of geopotential height (green), potential temperature (blue) and wind speed (barbs) at a pressure level of 700 hPa (top) and 850 hPa (bottom) for case D (14 April 2007), 18:00 UTC. Right: Geopotential height and relative humidity for the same time, at a pressure level of 700 hPa (top) and 500 hPa (bottom). The flight track is indicated as a red line.

ACPD

9, 15125–15179, 2009

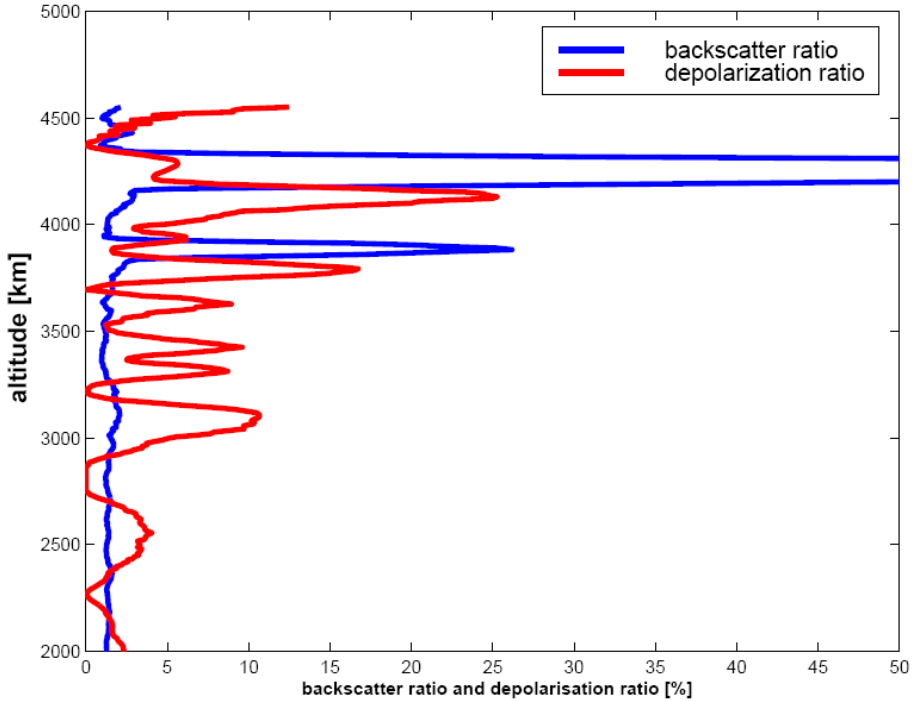

Fig. 15. Profiles of backscatter and depolarization ratio of case D (14 April 2007) at 16:18:45 UTC.

ACPD
9, 15125–15179, 2009